Mapping Samudra Tapu glacier: A holistic approach utilizing radar and optical remote sensing data for glacier radar facies mapping and velocity estimation

Sahil Sood [a], Praveen K. Thakur [a,*], Alfred Stein [b], Vaibhav Garg [a], Ankur Dixit [a,c]

[a] *Indian Institute of Remote Sensing (IIRS), Dehradun, Uttarakhand 248001, India*
[b] *ITC, the University of Twente's Faculty of Geo-Information Science and Earth Observation, Enschede, the Netherlands*
[c] *Indian Institute of Technology, Delhi, India*

Abstract

Himalayan glaciers have shown more sensitivity and visible changes to the climate change and global warming in the last 150 years. The highly rugged topography and inaccessible remote areas makes satellite images as the most appropriate source of information retrieval. We performed remote sensing based glacier change study for Samudra Tapu glacier, located in the Chandra basin of North-West Himalaya. In the present study, the capabilities of both optical and microwave remote sensing data was analysed in glacier change study in terms of its coverage, shift in equilibrium line altitude (ELA) and surface velocity over a period from 2000 to 2021. Multi Sensor (RISAT-1, Sentinel-1) time series of C-band SAR data along with a object oriented classification technique were used to identify different glacier facies such as percolation facies, icefalls, bare ice facies, refreeze snow and supraglacial debris. These classified maps were also used to detect the snow line and firn line along with ELA, aided with elevation information from digital elevation model (DEM). It was identified that more than 50 % of the total glacier area still lies into accumulation region. Further, we estimated the glacier surface velocity using Differential Interferometric Synthetic Aperture Radar (DInSAR) technique using European Remote Sensing Satellite (ERS-1/2) tandem data of 1996. High value of coherence was observed from the SAR return signal for one-day temporal difference. A mean velocity of 17–24 cm/day was found for the months of March and May 1996, highest flow rates were seen in the high accumulation area located in the Eastern and Southern Aspect of glacier. Spatial analysis of velocity patterns with respect to slope and aspect show that high rates of flow was found in southern slopes and movement rates generally increase with increase in slope. Feature tracking approach was used to estimate the glacier flow for long term and seasonal basis using optical and SAR datasets (IRS-1C, 1D PAN, Landsat-7, 8 PAN, and TANDEM-x) during 1999–2020 period. The results suggest that glacier flow varies with season, i.e., high velocity during spring-summer season, as compared to late summer or winter and, the rate of ice flow changes over the years. The mean glacier velocity reduced to 49.5 m/year during 2013–2020 time, as compared to 67.67 m/year during 1999–2003 time. These results of reducing glacier velocity and changing snow line altitude indicates enhanced glacier's melt rate and overall negative mass balance for Smudra tapu glacier.
© 2022 COSPAR. Published by Elsevier B.V. All rights reserved.

Keywords: Polarimetric SAR; Glacier facies; ELA; Glacier velocity; DInSAR; RISAT-1

1. Introduction

Glaciers are critical indicators of climate change as they can provide the signal of long-term changes in the atmo-

sphere. After the little Ice Age and in recent years due to global warming, glaciers are reported to be melting at a much faster rate (Eriksson et al., 2009; Lee et al., 2021; Dixit et al., 2021). This excessive melt can lead to certain hazards such as Glacial Lake Outburst Floods (GLOF), flash floods, avalanches in the mountainous regions and sea level rise, which causes threat to the coastal communities (Harrison et al., 2018; Zhang et al., 2021). Glaciers are perennial source of freshwater for agricultural, industrial and domestic use, especially in Central and South Asia (Singh and Singh, 2001). Himalayan-Karakoram glaciers cover an area of about 40,800 km^2 (Bolch et al., 2012). Most of the Himalayan glaciers are located in temperate regions of the world (except few glaciers in Karakoram Range, which are characterized by cold climate type), thus are receding at a much faster rate than the world average (Lee et al., 2021). Therefore, mapping, monitoring and inventorying changes in the Himalayan glaciers is very important. In-situ measurements provides valuable information about health of a glacier, but are sparse and expensive in vast Himalaya (Azam, 2021). Thus, a very little information in digital form is available for Himalayan glaciers (Frey et al., 2012). Furthermore, due to large spatial extent, inhospitable climatic conditions and inaccessible rugged terrain, remote sensing is an alternative approach, which can be used to monitor these ice masses. Remote sensing has provided an important tool for monitoring changes in glaciers such as, glacier area, advance and retreat of glaciers snout, Equilibrium Line Altitude (ELA), changes in the mass balance, and formation of supraglacial lakes (Berthier et al., 2007; Frey et al., 2012; Wagnon et al., 2007; Zhou et al., 2019; Bisset et al., 2020; Gaddam et al., 2022). Remote sensing methods can be used to estimate the velocity of the glacier, which can be used for estimating ice discharge (Hu et al., 2014; Kumar et al., 2011; Luckman et al., 2007; Scherler et al., 2008; Sattar et al., 2019; Yellala et al., 2019; Patel et al., 2021; Thakur et al., 2021).

Glacier facies are found due to spatial variations of glacier ice physical characteristics, which are easily seen in SAR data in the form the dry snow zone, percolation zone, wet snow, superimposed ice and bare ice zone (Benson, 1961, 2001; Benson et al., 2007). Mapping different glacier facies helps to determine the accumulation and ablation zones of the glacier i.e. the regions where glacier experiences gain and loss in their mass, an important factor towards monitoring of glacier's health. These in turn help us to determine the altitude of snow line and firn line, and finally the ELA, which is an important indicator of glacier mass balance and climate change. Bhardwaj et al., (2015) used Landsat-8 OLI and TIRS data for the characterization of glacier facies, however, this technique require a cloud free images of end of ablation season so that the glacier facies are clearly visible. Using optical data for glacier facies mapping has certain limitations such as cloud cover is prominent in these regions while a scene with minimum snow cover is required for the ice zonation mapping.

SAR systems has capability of penetrating clouds, thereby, are of considerable interest for snow cover and glacier monitoring. Distinct glacier facies like dry snow, percolation and wet snow (See Fig. S1A and S1B of supplementary data) are visible using SAR images of different seasons (Patrington, 1998, Rau et al., 2000). It is reported that target decomposition of fully polarimetric RADARSAT-2 image was useful to discriminate between wet snow and ice thus snowline was easily detected (Huang et al., 2011; Winsvold et al., 2018). Fully polarimetric ALOS/PALSAR data was also reported to be useful to discriminate between wet snow and other scatters in mountainous regions (Singh et al., 2014). Therefore, we have evidence that there is variation in the amount of backscatter and the scattering mechanism that can be used to identify various glacier facies. Higher reaches of glacier mainly consist of compressed dry snow or ice and experiences no or little melting even in summers therefore, comes under the dry snow region (Paterson, 1994). The volume scattering is dominant in dry snow region and any variation in the backscatter is due to the difference in the snow grain size (Patrington, 1998). Moving downslope there is transition in the snowpack conditions, as it changes to firn, the wet snow that probably survived the entire summer without being transformed to ice (Paterson, 1994). In the percolation facies, water percolates into snow upto a certain distance before it refreezes and form ice lenses and pipe like structures called ice glands (Patrington, 1998). Percolation facies backscatter high values especially in winter months due to these ice lenses, however, there is a drop in backscatter values as the surface becomes wet (König et al., 2001). Further, in the lower reaches of an accumulation zone, snow experience melting and refreezing that form wet snow facies. In percolation and wet snow facies, the scattering will differ from volume scattering in winter season to surface scattering in ablation season (Patrington, 1998, Rau et al., 2000). Ablation region is the lowest part of the glacier that experience negative change in the mass balance. This region consists of bare ice facies. In winter season, these bare ice facies covered with seasonal dry snow, those are transparent to microwave frequencies used, act as a specular reflector. However, in summer the scattering of bare ice appears higher than wet snow facies due to presence of melt water (Patrington, 1998). Mapping of glacier facies can be used to define firn line (i.e. altitude separating dry firn from wet snow), the ELA and snow line (i.e. the lowest altitude where wet snow is present at the end of ablation season; Huang et al., 2011). The yearly precipitation and the melting of the snow affect the ELA, but the firn line is relatively a longer timescale phenomena and not much affected by these yearly variations. Whereas, a permanent shift in the ELA will have an effect on the firn line, which in turn will have a pronounced effect on mass balance of the glacier (König et al., 2000; Rau et al., 2000).

Dry snow zones are found in cold polar glaciers (Benson 2001) and does not exists in most of the temperate glaciers found in Himalayas. The glacial ice remain at melting point
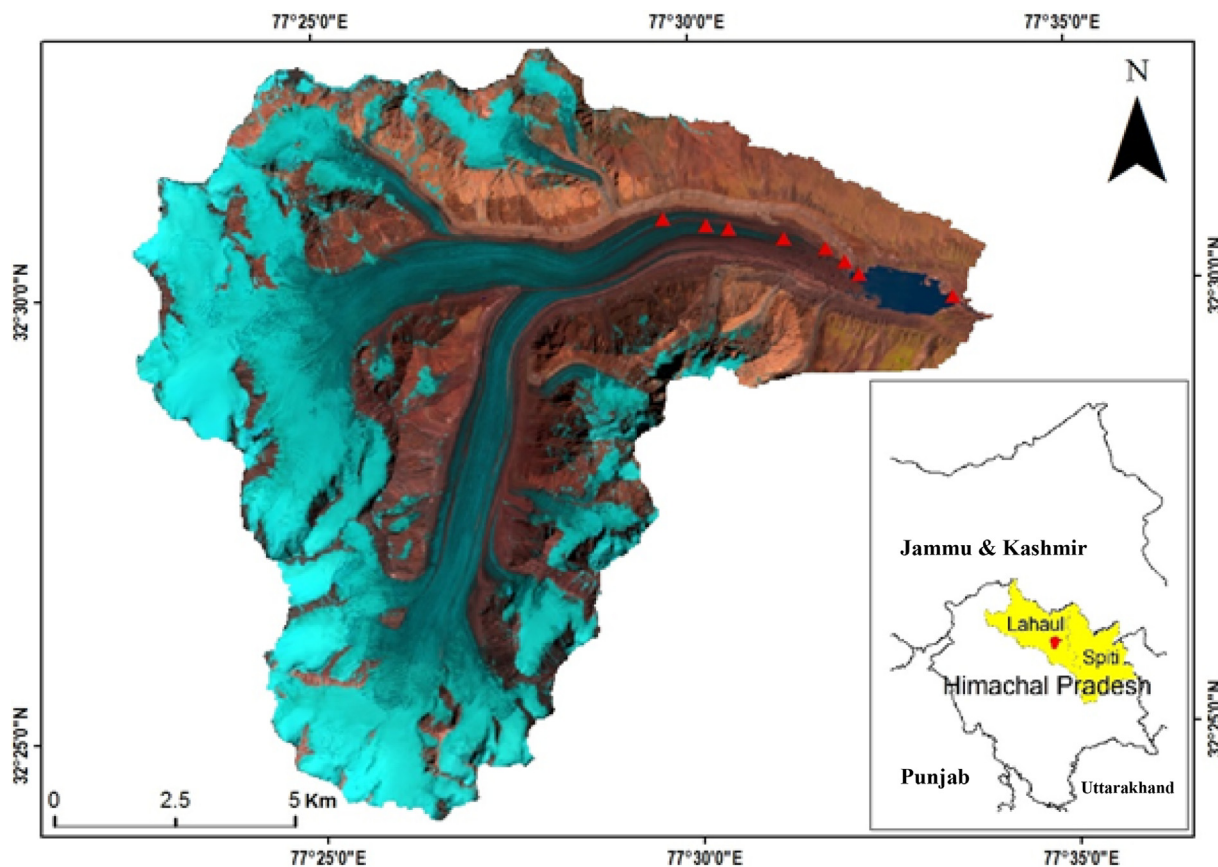
Fig. 1. Samudra Tapu glacier located in Chenab basin Himachal Himalayas (false colour composite) Landsat image (30-August-2015). The red triangles mark the position of the GPS points collected during the field visit.

for the most part of the year except winters for a temperate glacier. Superimposed ice is formed when firn is below 0°C, which is not the case for temperate glaciers thus equilibrium and snow line coincide with no superimposed ice zone (Paterson, 1994). Furthermore, wet snow line is coincident with the 0° isotherm subsurface position of the previous year's accumulation and has no effect on SAR backscattered properties, thus cannot be detected (Patrington, 1998). Percolation and wet snow facies collectively form the accumulation zone of the glacier and only surface melting happen in these regions. The necessary condition for a region to be classified as wet snow zone is that all the deposited snow of the winter accumulation should have melted away by the end of summer (Paterson, 1994). In the end of summer, both percolation and wet snow areas are melting, thus we get similar backscatter characteristics, therefore percolation and wet snow facies were treated together as percolation zone.

Glacier surface velocities are indicators of glacier mass balance and can be used to understand glacier dynamics (Zongli et al., 2012; Mandal et al., 2020). The current methods of estimating glacier flow are: i) SAR interferometry or DInSAR, and ii) Feature or offset tracking. The phase difference between two SAR acquisitions can provide the topographic information as well as the surface deformations, called as interferometry and, can be used to estimate glacier velocity. Interferometric SAR (InSAR) has a precision of few millimetres, but highly dependent on the phase coherence between two acquisitions. Moreover, the displacement values are not calculated in plane orthogonal to the radar Line Of Sight (LOS) (Gourmelen et al., 2011). Furthermore, it is constrained with limited number of scenes at a certain time. An alternative approach is feature of offset tracking, which uses a set of high resolution coregistered SAR or optical satellite images and uses cross-correlation techniques to detect identifiable features like crevasses and determines the rate of flow of glaciers (Giles et al.,2009; Singh et al., 2021). The feature/offset tracking results can be further used for the validation of DInSAR derived velocity estimates.

Ice motion controls the rate at which ice is transported from accumulation to ablation area (Paterson, 1994). By identifying the various glacier facies, we can determine the accumulation and ablation areas. Using the estimated surface velocities, we can determine the rate of ice flow from the region of accumulation to ablation. Therefore, the objectives of this study were to identify and map the different glacier facies using multi-temporal and target decomposition of SAR datasets; determining the equilibrium line altitude (ELA) and hence determine the
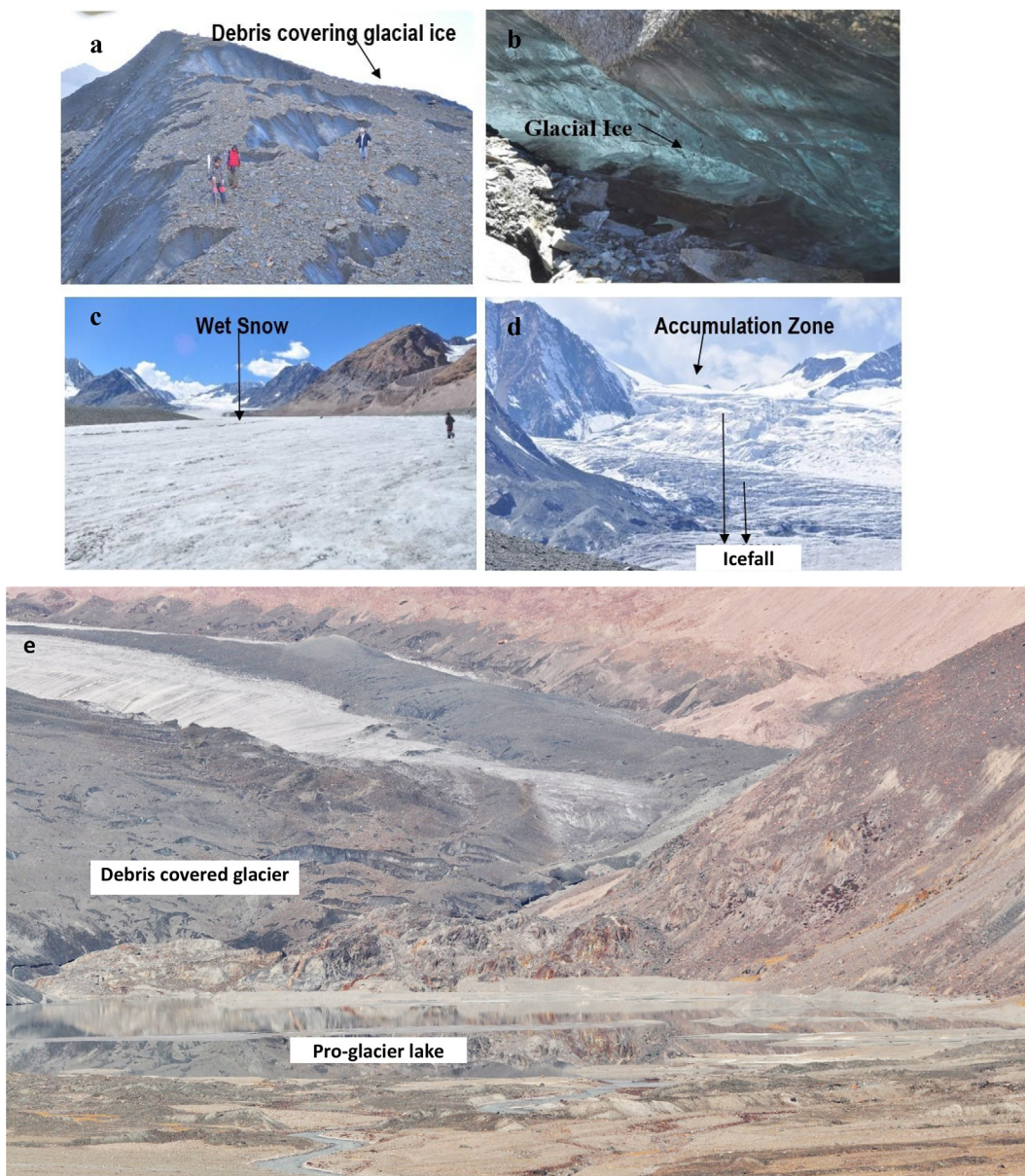
Fig. 2. Photographs taken during the field visit a) Debris covered glacial ice area near the snout b) Glacial ice c) Wet snow (classified as refreeze snow) in the lower middle ablation area d) Patches of ice walls and accumulation zone (classified as percolation facies) and e) Front part of Smudra Tapu glacier, with a pro-glacier lake, and debris covered lower ablation zones.

accumulation and ablation zones of the Samudra Tapu glacier; estimating the glacier velocity using both SAR and optical images.

2. Study area and data sources

2.1. Study area

This study focuses on the Samudra Tapu glacier which is located in the Great Himalayan range of North-West Himalaya; district Lahaul Spiti in the northern state of Himachal Pradesh. The location and features of study glacier are shown in Fig. 1 with Landsat-8 multi-spectral data. The accessibility to Samudra Tapu is through Rohtang

pass and Kunzum Pass at an altitude of 3915 m and 4551 respectively. The region consists of intersecting mountain ridges and is heavily glaciated due to heavy snowfall during the winter season. Most of the precipitation occur in the form of snow because of very cold semi-arid glacial climate (Shukla et al., 2010).

Samudra Tapu glacier is influenced by two weather systems i.e. mid latitude westerlies, and Indian south-west monsoon. The mid latitude westerlies are responsible for the Western Disturbances that precipitates most of the snow over this region. The glacier forms a cirque at higher elevations and flows like a valley glacier in the lower altitudes. The flow direction of the main trunk is in the West-East direction, whereas, the 2nd major branch of

glaciers moves in South-North direction. It is confined between latitudes 32°24′0″N to 32°32′45″N and longitudes 77°22′30″E to 77°32′30′′E with elevation ranging from 4200 to 6100 m amsl. The glacier has pro-glacial lake fed by the seasonal snow and glacier melt water, which contributes to the Chandra River (Fig. 2). There is a change in shape, size and orientation of the lake with respect to the change in snout over the years, and this lake expansion is cause of some concern in the downstream (Kulkarni et al., 2006; Dhar et al., 2010). Although it is noted during fieldwork that this pro-glacier, lake has a clear unobstructed outflow channel and wide valley in the downstream, making it less susceptible for glacier lake outburst floods (GLOF).

2.2. Data sources

The present work has utilized a number of remote sensing datasets from different sensors to fulfil the objectives of this study. The RISAT-1 MRS and Sentinel-1 datasets were used for the identification of glacier facies by multi-temporal SAR data. Fully polarimetric ALOS/PALSAR and RADARSAT-2 datasets were used for the purpose of target decompositions of SAR data. ERS 1/2 Tandem images with one day temporal resolution was used for obtaining horizontal displacement using InSAR techniques. Co-registered optical and SAR images of Landsat-5, 7 and 8, IRS-1C, IRS-1D, Sentinel-2, ASTER, TanDEM-X and RISAT-1 datasets were used for feature tracking. In this work, we have used Shuttle Radar Topography Mission, SRTM-30 m DEM (SRTM, 2015). The global glacier velocity data from ITS_Live data products (Gardner et al., 2019) are also used to compare the derived glacier velocity as per our study.

The details of these datasets used in the present study are provided in the Table 1 with their dates, spatial resolution and other features. The remote sensing based analysis require verification of derived parameters, therefore, a field work of the Samudra Tapu glacier was performed during 1st week of October 2013, with some of the field photographs as shown in Fig. 2. During the field survey, the photographs of the glacier features, global positioning system (GPS) based ground control points and snow probe data on lower ablation part of glacier were collected. During to fieldwork, following glacier facies were identified; supraglacial debris, bare ice, refreeze wet snow (snow falling during late ablation season and undergoing cycles of melting and freezing), icefalls and, percolation zone which is permanent snow found above the ELA.

3. Methods

The detailed methodology flow chart of the present study is provided in Fig. 3. The present study methods has been divided into two broad parts; a) Glacier facies mapping using multi-temporal SAR data and, target decomposition of fully polarimetric SAR data to support glacier facies mapping; b) Glacier velocity estimation using SAR and optical

remote sensing data. The detailed description of each method is provided in the subsequent sub-sections.

3.1. Discrimination of glacier facies using multi-temporal SAR images

Glacier facies show variation in the amount of backscatter in different seasons, thus can be identified using multi-temporal SAR images (Patrington, 1998). As SAR backscatter values depend on the incidence angle and the wavelength of the signal therefore the acquired images should be of the same sensor with identical geometry so that the difference in the backscatter is only because of variation in the season. The SAR images must be georeferenced and terrain corrected to remove the effects of layover and shadow. These SAR images are filtered to remove speckle noise. For this purpose, Equivalent Number of Looks (*ENL*) is estimated using the smooth part of the image where variance of signal is low, thus the main contribution is from speckle. The moraine-dammed lake at the snout was used to calculate the *ENL* number (Lee and Pottier, 2009) and was calculated using equation (1).

$$ENL = \frac{1}{Coff.ofvariation^2} \quad (1)$$

These images were filtered using Lee filter. The areas accounting for layover/shadow were removed from the images. After pre-processing, these SAR images were stacked, creating a single channel colour composite of three bands in which blue channel is assigned to winter image, red channel to early summer image and green channel to late summer image to display the multi-temporal signatures as distinctive colours (Patrington, 1998). These distinct tones represent different glacier facies. In the present study, the RISAT-1C-Band Dual Polarisation datasets were used for glacier facies mapping for the year 2013. However, the Sentinel-1C-band VV polarisation datasets were used for the years 2016–2021, as listed in the Table 1.

3.2. Target decompositions

Target decomposition could be used to determine some of the physical properties of the target under observation (Cloude and Pottier, 1997). A point target in case of monostatic fully polarimetric SAR data can be characterized by five parameters, three amplitudes and two relative phase therefore is useful for classification and segmentation (Singh et al., 2011). Glacier facies have different scattering mechanisms, thereby using target decompositions we can express the scattering matrix of fully polarimetric SAR data as combination of scattering response from different type of glacier facies. In this paper incoherent H/A/α Decomposition (Cloude and Pottier, 1997) has been used for retrieval of scattering elements. The incoherent decompositions use the second order statistics of polarimetric information and decomposes the coherency matrix as incoherent sum of scat-

Table 1
List of satellite data and their specification used for this study.

Satellite	Band	Polarization	Resolution (m)	Date
RISAT-1	C	HH,VV	18	05/01/2013
				15/04/2013
				18/08/2013
				01/12/2013
Sentinel-1	C	VV	20	Multiple dates from 2015 to 2021
ALOS/PALSAR	L	HH,HV,VH,VV	25	12/04/2011
RADARSAT-2	C	HH,HV,VH,VV	10	27/01/2014
ERS-1/2 Tandem	C	VV	25	28/03/1996
				02/05/1996
				29/03/1996
				03/05/1996
TanDEM-X	X	HH	5	25/09/2013
				28/10/2013
Landsat-7 ETM+	PAN	N/A	15	09/07/1999
				20/08/2000
				28/06/2001
				02/08/2002
Landsat-8 OLI/TIRS	PAN	N/A	15	23/07/2013
				11/08/2014
				30/08/2015
				16/08/2016
				04/09/2017
				22/08/2018
				10/09/2019
				12/09/2020
Sentinel-2 MSI	Band-4	NA	10	28/08/2018
				28/08/2019
TERRA/ASTER	VNIR	N/A	15	08/09/2004
				30/09/2006
IRS-1C	PAN	N/A	5	25/08/2000
				15/08/2002
				01/07/2006
				26/06/2007
IRS-1D	PAN	N/A	5	03/07/2003

tering power of a distributed target (López-Martínez and Pottier 2021). As the natural targets such as glacier facies can only be characterized statistically (Huang et al., 2011). The target decomposition of ALOS PALSAR and RADARSAT fully polarimetric SAR data was carried out to support the identification of glacier facies. There was a considerable amount of layover and shadow in the ALOS/PALSAR dataset because of a lower incidence angle in comparison the RADARSAT-2 dataset, which were acquired at a higher incidence angle, these distortions were masked out from the decompositions. Once the glacier facies were identified, the decomposed images were further classified using image classification techniques to map the boundaries and area of glacier facies. The details of image classification methods is given in the next section.

3.3. Object oriented classification

Object oriented classification has been used to classify the glacier facies map. This method consists of dividing the image into homogeneous patches called as objects, before these objects are assigned to a certain class based on the statistical homogeneity. We used eCognition software to perform the segmentation to create the objects in the image. Multiresolution segmentation was done to divide the image into homogeneous patches. In segmentation stage a few parameters should be carefully chosen such as scale, shape and compactness. We chose the scale to be the maximum allowed heterogeneity in the image objects; as higher the shape criterion least it is influenced by spectral homogeneity for generating image objects. Compactness is only active when the shape parameter is larger than 0 (Definiens Developer, 2012). Nearest neighbourhood classification is based on user defined functions of objects and uses a set of different classes to assign membership values. Sample image objects are chosen with their label and then the algorithm compares an image objects to already existing sample and determines whether it belongs to a particular class (Definiens Developer, 2012).

3.4. Differential SAR interferometry (DInSAR)

Glacier flow is directly related to its melt because as the rate of flow is reported to be in association with ice discharge (Mandal et al., 2020). We used SAR interferometric technique as it can detect centimetre scale of deformations
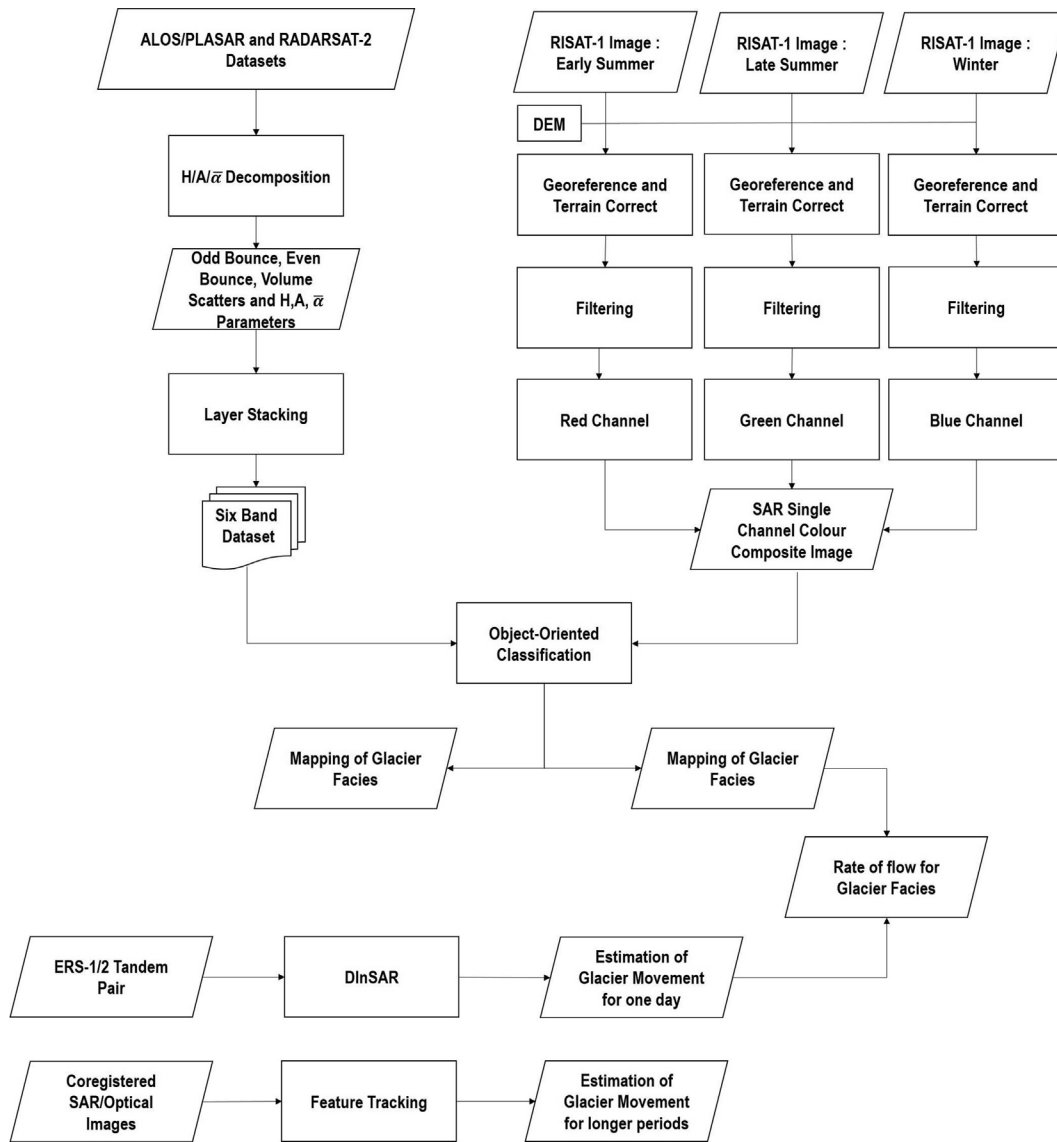
Fig. 3. Systematic workflow of the used methods.

(Reigber et al., 2003). SAR signal carries the information of radar backscattered intensity and phase. The value of phase depend on the radar wavelength and roundtrip path (Kumar et al., 2011). InSAR uses the phase information from two SAR images having same wavelength and covering same area. Coregistration aligns these images and pixel by pixel phase difference is calculated (Li et al., 2008). A simulated interferogram by removal of the topographic component of the phase using an external Digital Elevation Model (DEM) is called as DInSAR. In this work, we have used SRTM-30 m DEM for image co-registration as well as to remove topographical phase. Due to the flat earth effect the fringe density is high, so it is necessary to flatten the interferogram before the process of unwrapping. Coherence is the degree of quality of the interferometric phase and is estimated using flattened interferogram and the intensity image. Coherence is unitless and its value ranges from 0 to 1, values less than 0.25 are not suitable for phase

unwrapping (Small et al., 1993). Phase ambiguities are removed by the process of phase unwrapping and the correct multiples of 2π are restored to each pixel. Orbital refinement is done to remove the phase offsets over the non-moving areas. For this purpose, a Ground Control Point (GCP) file is used. Afterwards, the unwrapped phase information can be used for transformation into height or displacement values. For the estimation of the displacement values, the key factor is the angle α i.e. the angle between the radar Line Of Sight (LOS) and the direction of the glacier motion. It can be calculated by the equation (2) (Li et al., 2008).

$$coscos\alpha = coscos\theta sinsinS + sinsin\theta coscosScoscos\varphi \qquad (2)$$

where θ is the incidence angle, S is the surface slope, φ is the relative azimuth angle between the two directions. The magnitude of the displacement D can be derived using the equation (3) (Li et al., 2008).

$$D = \frac{\Delta l}{cos cos \alpha}$$

$$= \frac{N_{fr} \times \lambda}{2 \times cos cos \theta sin sin S + sin sin \theta cos cos S cos cos \varphi} \quad (3)$$

where Δl is the displacement along the LOS, λ is the wavelength, N_{fr} is the number of fringes along the area of interest. For the estimation of the glacier flow, an assumption is made that glacier flows parallel to the surface.

3.5. Feature tracking

Although DInSAR maps the glacier velocity at a centimetre level accuracy, this approach has certain limitations (Strozzi et al., 2002). For glacier movement SAR interferometry has constraints of limited number of scenes at a certain time (Giles et al., 2009). It is highly dependent on coherence; a large temporal resolution between two SAR acquisitions can lead to total loss of coherence. Furthermore, the interferometric velocity is representation of a certain time and extrapolation to retrieve annual velocities is difficult (Scherler et al., 2008). An alternative approach for deriving glacier velocity is feature tracking (Zongli et al., 2012). Feature tracking can use SAR and optical datasets to analyse glacier flow over longer times (Scherler et al., 2008). There are some prerequisites of feature tracking: a) Surface features must be detected in both pre-event and post-event images; b) The datasets must be accurately coregistered; c) The spatial resolution of images must be less than the displacement (Huang and Li, 2011). Coregistration is the pixel by pixel matching of the pre-event and post-event images. Correlation is the degree of matching in the master and slave images and, is given by (Evans, 2000). Correlation peak is identified in the window defined by the user in both pre-event and post-event images and shift is calculated in north–south and east–west directions. Then the displacement is calculated as follows:

$$D_h = \sqrt{(R_x \Delta x)^2 + (R_y \Delta y)^2} \quad (4)$$

Where R_x and R_y are the pixel spacing in x and y directions. For SAR data they are represented as azimuth and slant range directions. Feature tracking for SAR datasets was carried out using amplitude tracking. It is based on examining the backscatter intensities. Amplitude tracking tool is available in SARscape module under ENVI software. The input required is two radar scene pre-event as master and post-event as slave. TanDEM-X, RISAT-1 MRS datasets were used for amplitude tracking. Firstly, the SLC data sets were co-registered with sub-pixel level accuracy. According to Racoviteanu et al., (2007) SRTM DEM is sufficient to analyse glacier flow with low slope, hence used in this technique. Thereafter amplitude tracking is carried out using cross-correlation method. We get shift in number of pixels in range and azimuth direction these have to be and multiplied with corresponding pixel spacing to transform the shift into metric units.

Feature tracking technique was implemented to calculate surface velocities using sub-pixel correlation of acquired images using freely available software, Coregistration of Optically Sensed Images and Correlation (Cosi-Corr), which can be downloaded through the URL: https://www.tectonics.caltech.edu/. The software package is an IDL based module for ENVI by RSI. The optical images used in this study are panchromatic bands of 15 m resolution of Landsat-8 OLI/TIRS and Landsat-7 ETM, IRS-1C&1D panchromatic band 5 m resolution and ASTER band 3 N with 15 m resolution. The images selected for this study were having minimum cloud and snow cover, so that the trackable features can easily be identified. These datasets must be coregistered and orthorectified so that the measurements made are in same scale. The Landsat images can be freely downloaded from https://earthexplorer.usgs.gov/ that are already georeferenced and orthorectified, so the process of orthorectification was carried out only for ASTER and IRS images. The procedure of orthorectification relied upon automatic generation of GCP's. A precise set of GCP's was generated from an already orthorectified master image. SRTM 30 m DEM was used for orthorectification. Leica Photogrammetry Suite (LPS) was used for the orthorectification of IRS-1C&1D datasets. ASTER images were orthorectified using Cosi-Corr module. Region of interest i.e. the study area was masked out to reduce the computational time. In case of Landsat and ASTER image pairs, measurement of large scale displacements was done with a moving window size of 64X32. A step of 2 pixels was used so that the ice flow maps are resampled at 30 m. A moving window size of 128X64 with step of 6 pixels was used for IRS-1C&1D datasets, so as to keep ice velocity at spatial resolution of 30 m. After performing the correlation, we have three outputs: a north–south displacement, an east–west displacement and signal to noise ratio. A vector field is generated using the east–west and north–south components of velocity field. All pixels having SNR less than 0.95 and displacement greater than 190 m were discarded. The velocity vectors are properly aligned except for the areas having snow in either of the master or slave image. The Eulerian norm of the displacement is calculated using east–west and north–south components to find the resultant displacement. Most of the image pairs were having different time gaps thus the velocity values were converted to daily values using time difference of master and slave image, then converted to displacement per annum to draw a better comparison between the obtained results.

4. Results

4.1. Discrimination of glacier facies using multi-temporal SAR data

RISAT-1 Medium Resolution ScanSAR (MRS) datasets were used in this study to map glacier facies for the year 2013. The SAR images were combined from three

seasons: winter, early summer and late summer (Fig. 4 A to D). Out of these winter and late summer images define the maximum melt and freeze conditions. The timing of early summer and late summer image is critical as the snow extent deplete rapidly over the summer season. After the basic pre-processing of these seasonal SAR images, a colour composite is created using early summer image as red, late summer image as green and winter image as blue channel. This colour composite is able to highlight various distinct glacier facies (Fig. 4D). At higher elevations, purple colour is most dominant and they are interpreted as percolation facies. Here no or very little melting takes place in winter and but a cycle of day time melting and night time refreeze occurs in early and late summer, thus higher values of backscatter was found due to presence of frozen rough snow/ice, which is in the range of − 8 to − 2 dB (Fig. 4A). In addition, during the early summer, surface melting takes place even at higher reaches and the backscatter values drop to − 25 to − 20 dB, thereby, even higher reaches appeared relatively darker in Fig. 4B. During the late summer, due to complete melting of seasonal surface snow in the ablation area, only clean ice and debris covered ice is visible, thus giving less backscatter in ablation zone. Similarly, the time-series (2016–2021) of

Sentinel-1 SAR data has been used to generate the annual color composites (Figure-5) from year 2016–2021, interpret glacier facies maps and, same identified zones are used to estimate the snowline for a given water year.

The difference in the backscatter from the percolation facies in different seasons can be seen in the Fig. 6A. The anomalous appearance of green colour at higher altitudes as seen in the Fig. 4D is quite unusual. As suggested by Patrington (1998), it could be due to summer depth hoar development, rime frost development and high winter accumulation over the percolation facies. Fig. 4D shows purple colour and high backscatter feature at some places in the middle altitudes of the glacier. These regions were identified as icefalls using Survey of India (SOI) toposheets (1:50 000 scale, 52H/3, H/7) along with August time cloud free optical images; icefalls being a corner reflector gives higher returns in the range − 10 to − 2 dB. Bare ice facies are seen with a tint of green colour and is observed just below the percolation facies. Here melt is observed in late summer and early summer seasons, but melting does not takes place during winters. Low values of backscatter in the range − 25 to − 10 dB are seen here in all the seasons. In winters, the whole of the glacier is covered by seasonal dry snow, the incoming microwave radiations are transpar-
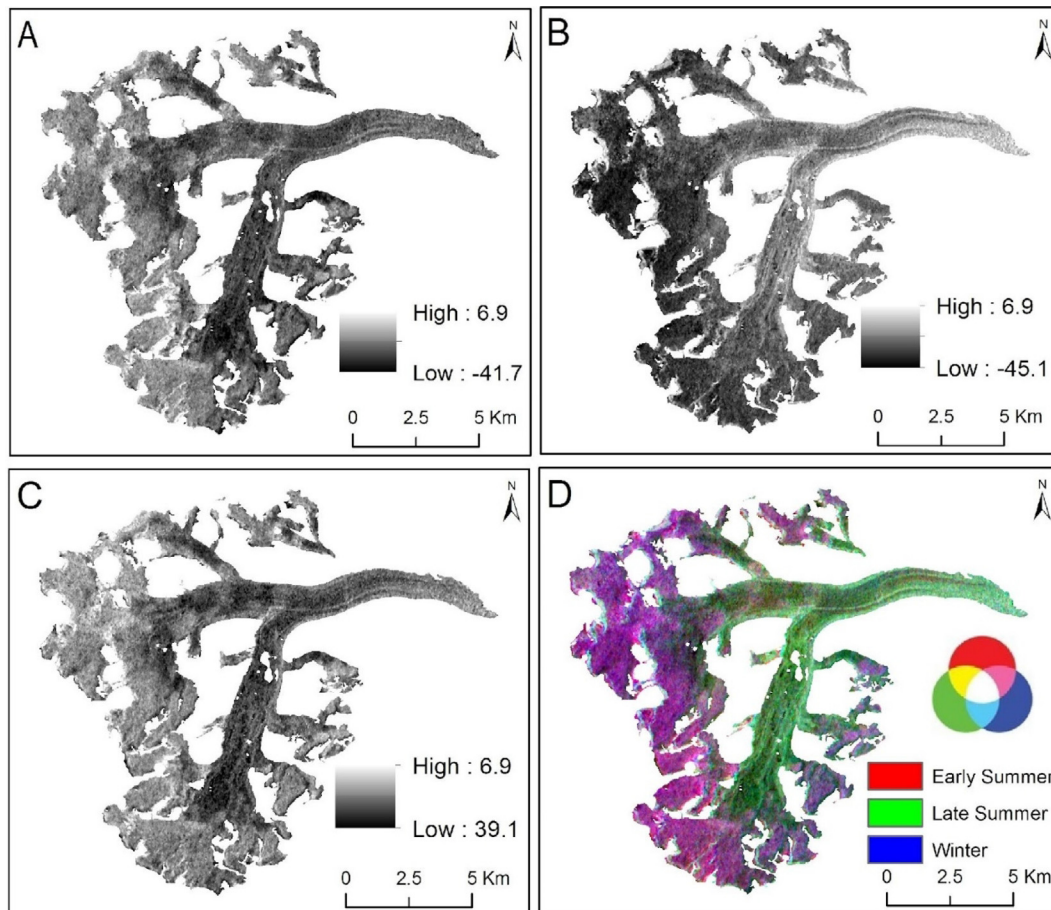

Fig. 4. A), B), C) Backscatter images with HH polarization for the date 15-April-2013, 18-August-2013 and 05-January-2013, D) Single channel RGB colour composite image using multi-temporal RISAT-1 MRS data with HH polarization.
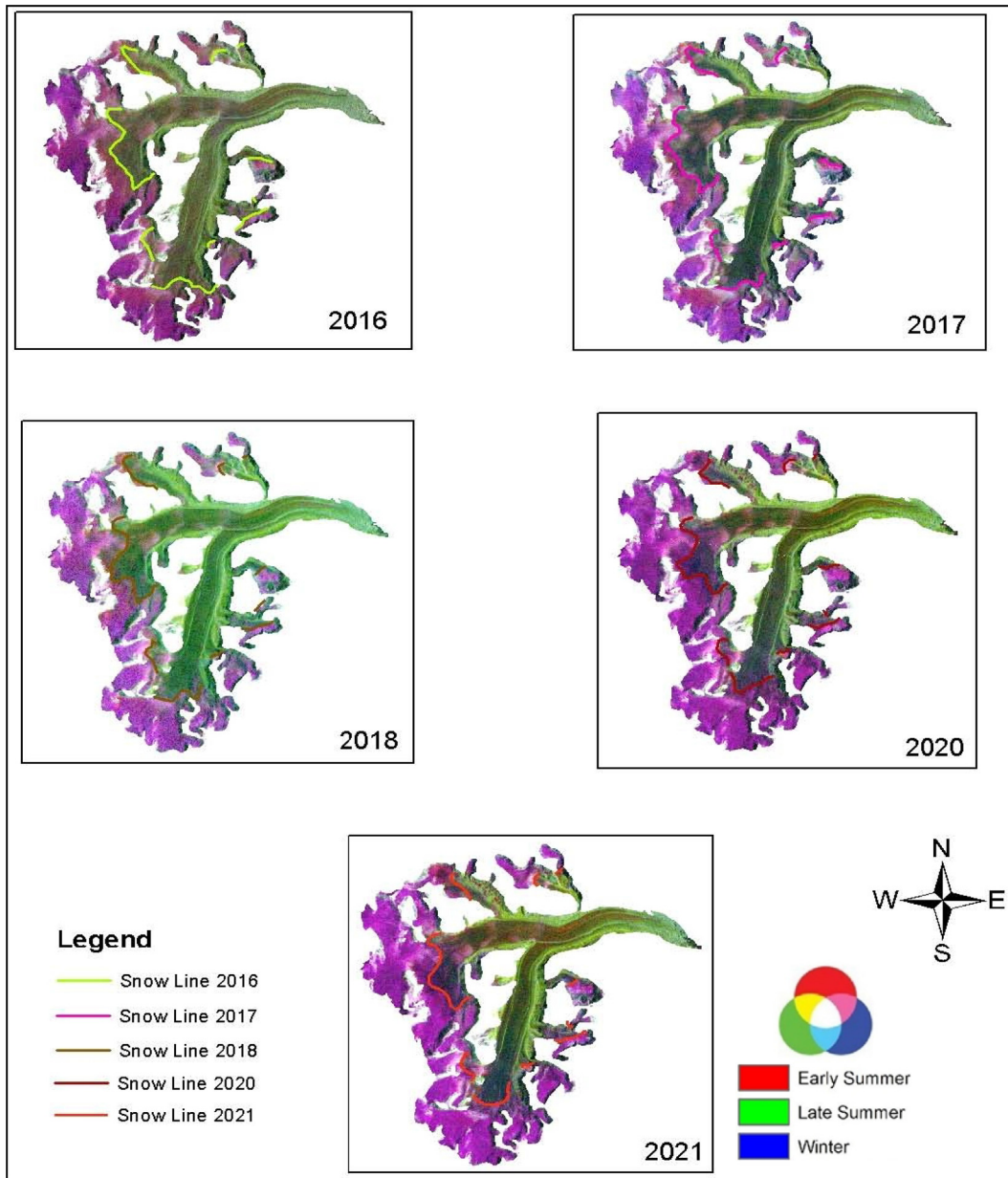
Fig. 5. Multi-Temporal Sentinel-1 (VV polarization) dataset colour composites from 2016 to 2021 and inferred snowline for each year.

ent to this dry snow and the backscatter comes from the glacial ice (a smooth surface) or glacier debris (rough surface), which reflects the radiations in a specular or diffuse manner causing low or higher backscatter to the radar antenna. In early summer, winter snow starts to melt and low backscatter is observed due to presence of melting wet snow. In late summer, melting of snow, firm and ice occurs during day and same refreezes into a rough crystalline ice form in the night. The RISAT-1 images were acquired in early morning, thus the backscatter comes through the rough glacial ice surface causing backscatter values to be slightly higher in late summer in comparison to winter and early summer images. Supraglacial debris can be seen as bright areas with green colour near the snout and moraines along the glacial ice. The detailed values of

backscatter from various glacier facies in different seasons of the years can be seen from the Fig. 6A.

4.2. Target decomposition of polarimetric data for glacier facies mapping

The ALOS/PALSAR and RADARSAT-2 images are processed in the following procedure: Firstly H/A/α decomposition is applied on the scattering matrix in SARscape module in ENVI software. This generates matrices, which indicate single bounce, double bounce and volume scattering for both decompositions and entropy H, anisotropy A and scattering angle α as secondary decomposition parameters. Then from these Single Look Complex (SLC)
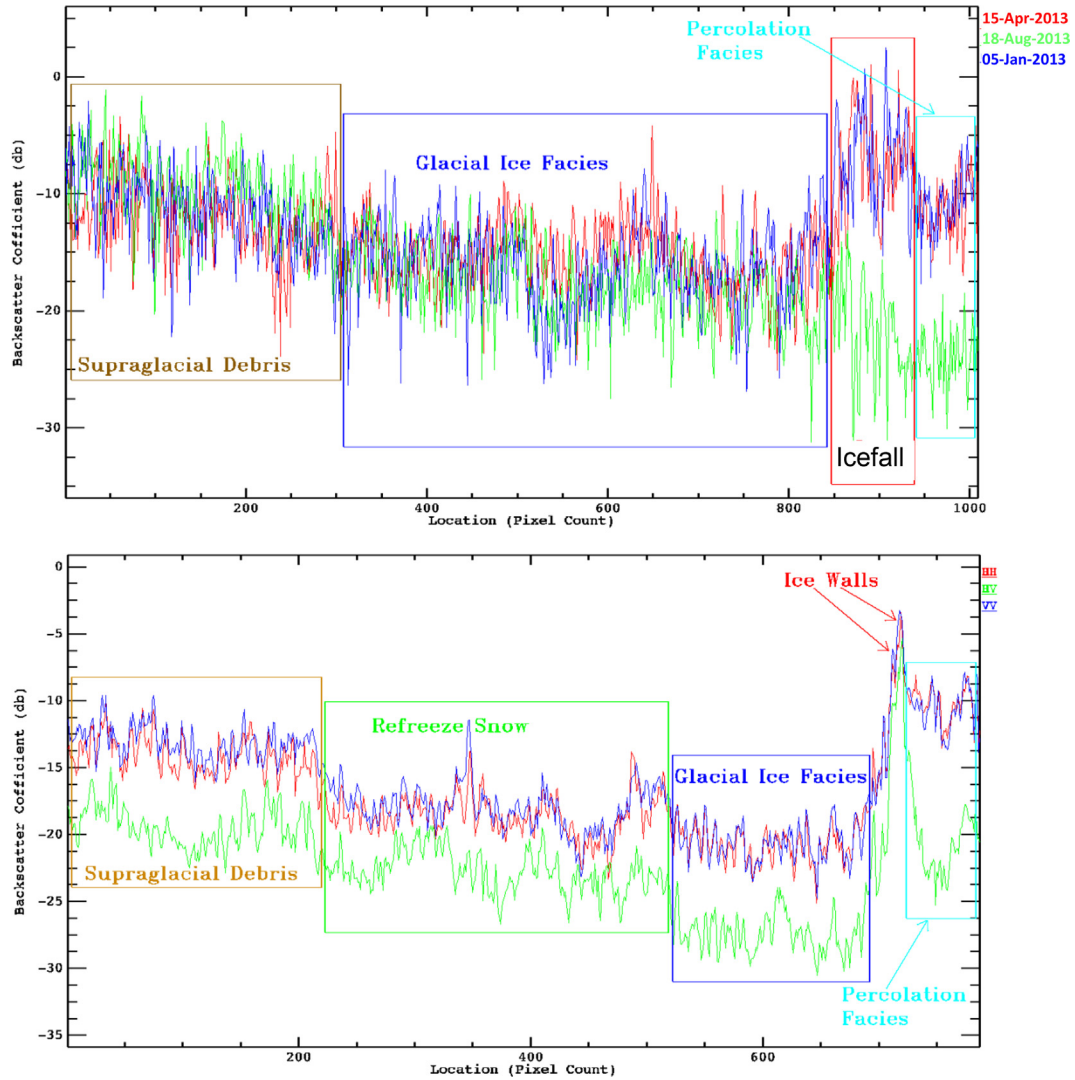
Fig. 6. **A)** RISAT-1 backscatter coefficient (HH) in different seasons of year 2013**B)** ALOS/PALSAR backscatter coefficient in various polarizations on 12 April 2011.

images, multi-look images were generated which were then georeferenced, as shown in Fig. 7A and 7B. There is difference in the decomposition results of two images as they are acquired using different frequencies at different time of year. Both ALOS/PALSAR and RADARSAT-2 images are acquired at the night-time so there is much more penetration as the snow surface is dry, low frequency like L and C-band microwave radiations are able to penetrate the dry snow, thereby underlying sub-surface features can be detected (Rott et al., 1987). In case of ALOS/PALSAR decomposition, we can see the presence of blue colour at high altitudes, which indicate surface scattering as the dominant scattering. The main polarimetric response from the snowpack is surface scattering in the L-band (Abe et al., 1990). Thus, there may be an area of permanent thick snow cover at higher accumulation zone, which forms the percolation facies. Since the HV component contribute to volume scattering, thus HH and VV components dominate in the percolation facies (Fig. 5B). The decomposition

results of RADARSAT-2 indicate the presence of green and purple colour at high altitudes. The C-band SAR signal are not able to fully penetrate the snow pack thus volume scattering takes place, purple colour indicate both surface and double bounce scattering mechanism because of the backscatter from the rough surface of old glacial firn (Fig. 7B). The surface undulations become more prominent in case of RADARSAT-2 data, as the C-band radiations have less wavelength in comparison to L-band data. Immediately below the percolation facies, we can notice white patches with tint of green colour scattered throughout the glacier. These can be identified as icefalls where all three scattering mechanisms are found. The Fig. 6B shows that HV component is at par with the HH and VV component in the regions of icefalls. Large patches of dark blue colour refer to bare ice facies (Fig. 7B). Thick layer of seasonal wintertime dry snow covers the glacial ice. The microwave radiations penetrate this winter dry snowpack and backscattered by the glacial ice, which can be seen as
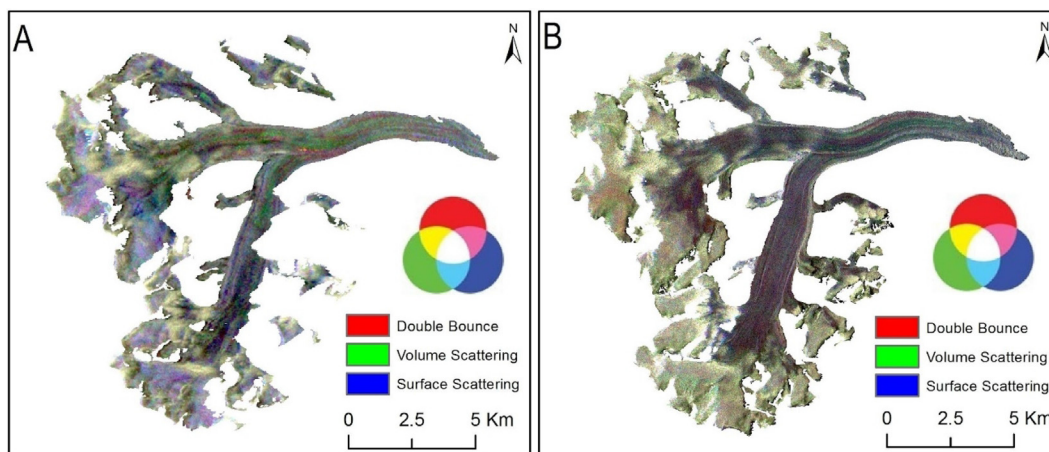
Fig. 7. H/A/α decomposition results **A)** ALOS/PALSAR 12-Apr-2011**B)** RADARSAT-2 27-Jan-2014.

dark grey tone in the corresponding backscatter image. Moving further downslope, some areas can be seen in green colour in Fig. 7A, 7B that indicate refreeze snow. The snowfall that occurs towards the end of ablation season (August-September) melts, refreezes into a rough crystalline solid, and is covered by dry snow in winter. It has a large component of surface scattering that can be seen in Fig. 7B. The refreeze snow is the slush which is formed by melting of fresh snow after the end of ablation season. Supraglacial debris covered areas are seen with red and blue colour in case of decomposition of ALOS/PALSAR datasets. The red colour corresponds to double bounce scattering, near the snout of the glacier patches. The blue colour patches indicate that surface or volume scattering comes from the wintertime snow accumulations or debris cover, which can be present in upper accumulation and lower ablation zones respectively. In case of decomposition of RADARSAT-2 datasets, the supraglacial debris can be seen with bright patches of blue colour (Fig. 7B and 8B). Thus, the decomposition of fully polarimetric SAR data was found very useful for identifying the type of scatters and different glacier facies.

4.3. Glacier facies mapping using SAR data classification

RISAT-1 multi-temporal colour composite image and six layers i.e., three layers of primary decomposition parameters of H/A/α decomposition, and secondary parameters such as scattering angle α, entropy H, anisotropy A layers were stacked for ALOS/PALSAR and RADARSAT-2 datasets. The composite was used as input for image classification. Firstly, the images were divided into segments using multi-resolution segmentation (object-oriented classification). For image segmentation eight equal weighted layers were used and anisotropy layer was assigned weightage of 0, as this parameter is only useful for entropy values greater than 0.7. The images were divided into homogeneous patches by varying the value of scale parameter and shape parameter. The compactness

parameters were not used as the glacier facies does not have any predefined regular structure. The identified glacier facies were used as feature classes to be considered for classification training dataset. As this technique is supervised classification thus the image objects in the segmented image are selected as samples using the sample editor tool for various classes. The mean values of layers are the object features considered for the feature space. From all of the object related features the feature space optimization tool selects the optimal object features which have best separation distance in the class separation distance matrix. Finally standard nearest neighbour classification algorithm is applied. The algorithm uses the set of samples of different classes to assign membership value. If the object is identical to the sample its membership value is equal to one otherwise the feature space distance has a fuzzy dependency. The classification results were having certain anomalies; a DEM was used to filter results in the following ways: i) In RISAT-1 datasets; the single band multi-temporal image shows percolation zone and icefall with similar colour so SRTM DEM was used to classify these regions as icefalls. Also the unusual appearance of green colour at high altitude as referred earlier was filtered with the help of DEM. ii) Classification results of ALOS/PALSAR and RADARSAT-2 datasets show some patches of high scattering appeared in the debris covered areas, especially near the snout of the glacier, which were similar to that of percolation zone. These were filtered using DEM. Finally, some wrongly classified patches were reclassified using the manual editing tool. SRTM DEM has estimated horizontal accuracy of 20 m so this error is inherent in the classification results as all the datasets were geocoded using SRTM DEM ("Shuttle Radar Topography Mission," 2015). Table 2 indicate acceptable values of classification accuracy and kappa coefficient for all datasets. The highest accuracy was achieved using the RISAT-1 SAR daatsets, i.e., 95.18 %.

RISAT-1 multi-temporal dataset for classification (Fig. 8A) were able to identify less number of classes in

Table 2
Accuracy and Kappa coefficient for the different classified images.

	RISAT-1 (Multi-Temporal)	ALOS/PALSAR (12–04–2011)	RADARSAT-2 (27–01–2014)
Overall Accuracy	95.18 %	89.66 %	93.22 %
Kappa Coefficient	0.92	0.85	0.89

comparison to the number of classes obtained from the classified decomposition from ALOS/PALSAR (Fig. 8B) and RADARSAT-2 (Fig. 8C) datasets. The classification of multi-temporal RISAT-1 data were able to identify mainly supraglacial debris, percolation and glacial ice facies (Fig. 8A). The region of icefalls in the ablation area were classified using DEM. In addition to these classes, refreeze snow and icefalls were also identified in the accumulation area.

Glacier facies varies across the glacier (Fig. 8A, B and C) thus spatial analysis of glacier derived classes was done with respect to altitude, slope and aspect. Almost entire supraglacial debris is limited between the altitudes 4175–5100 m (Fig. 9A). Percolation facies are found above 5100 m of altitude. Altitude of 5100 m marks the transition boundary between percolation and ice facies. Almost 90 % of supraglacial debris and glacial ice are found at low slopes of 0–15°. Slopes higher than 20° are found at high altitudes that have percolation facies and icefalls as dominant classes (Fig. 9B). More than 50 % of percolation facies are found in northern aspects that are least exposed to sunlight, and thereby least melting is observed in these zones. Almost 50 % of supraglacial debris covered area was found in northern slopes (Fig. 9C). This presence of debris over glacial ice insulates the glacial surface and slows down its melting (Collier et al., 2015).

4.4. Detection of firn line and snow line using classified data

Snow line is the lowest altitude at which wet snow zone is found or in other words, it is the highest altitude at which the annual snow survive until the end of ablation season. It changes with season and at the end of ablation, the snow line is equal to Equilibrium Line Altitude (ELA) for temperate glaciers (Paterson, 1994). Above the ELA, glacier has net gain in mass and below ELA it is a net loss over a year, thus ELA is used to estimate the net mass balance of the glacier (Adam et al., 1997). Firn line is the boundary between the glacial ice and the old firn from previous years and has a more stable position than snow line because the firn is denser form of snow that has lower melt rates (Jaenicke et al., 2006). Thus, the changes in firn line show variations of larger time scales (König et al., 2000). It is clear that snow line, ELA, firn line are useful for glacier health. In this study, we used two different approach of glacier facies mapping, one by using multi-temporal SAR data and other is polarimetric decompositions of fully

polarimetric SAR data. In the multi-temporal approach, we used the SAR datasets of different seasons. According to the study by Venkataraman, (2011) the transient boundary between the percolation and the bare ice facies using multi-temporal SAR datasets represent the snow line. We can say that using multi-temporal RISAT- 1 and Sentinel-1 SAR data snow line can be detected (Figs. 4, 5, 11 and 12). The boundary between percolation and bare ice represents snow line. As one of the images is of 18-August-2013 (Fig. 4B) that represents the end of ablation season (time of the year when snow line coincides with ELA and its position includes information about mass balance). The other approach we used was polarimetric decompositions of fully polarimetric ALOS/PLASAR and RADARSAT-2 datasets. The RADARSAT-2 image is acquired on 27-Jan-2014 representing the winter season, when whole of the glacier is covered by seasonal winter snow, which is dry in nature, and also transparent to the C-band SAR system. The firn which is formed by the accumulation of old snow layers, exhibits volume scattering. In the past SAR images were used for winter season equilibrium line detection. However, these findings were not supported through the ground based observation. The recent work suggested that these are firn lines rather than ELA (König et al., 2001). The snow line and firn line altitudes in the different branches estimated from the DEM is shown in the Fig. 10. The winter image of RADARSAT-2 shows the firn line, the transient boundary between the percolation facies and the bare ice facies or the icefalls (Fig. 11). The altitude of snow line and firn line vary throughout the glacier thus these are estimated separately in the different branch of the glacier. Fig. 11 shows snow line, firn line and contour line overlapped together. The estimated vertical accuracy is of 10 m for SRTM DEM thus the determined altitude lines have at least 10 m of inherent error ("Shuttle Radar Topography Mission," 2015). Further, it is the limitation of use of single date SAR data for estimation of snow or firn line altitude (Figs. 10 and 11). In this particular glacier, the transitional zone (between percolation and bare ice zone) is fairly rough (due to presence of crevasses) which would increase the backscatter and the surface would appear as percolation zone. Therefore, the firn line altitude, in the present study, is higher than the snow line altitude. Attributing to this limitation, snow line was underestimated in the present study.

4.5. Glacier velocity using SAR interferometry

Ascending pass SAR images (in pairs) of ERS1/2 for month of March and May with one-day temporal resolution were used to estimate surface velocity using SAR interferometry approach. A coherence threshold of 0.25 was used assuming small amount of displacement takes place along the glacier. Well distributed thirty-five GCP's were used in the process of orbital refinement. These unwrapped
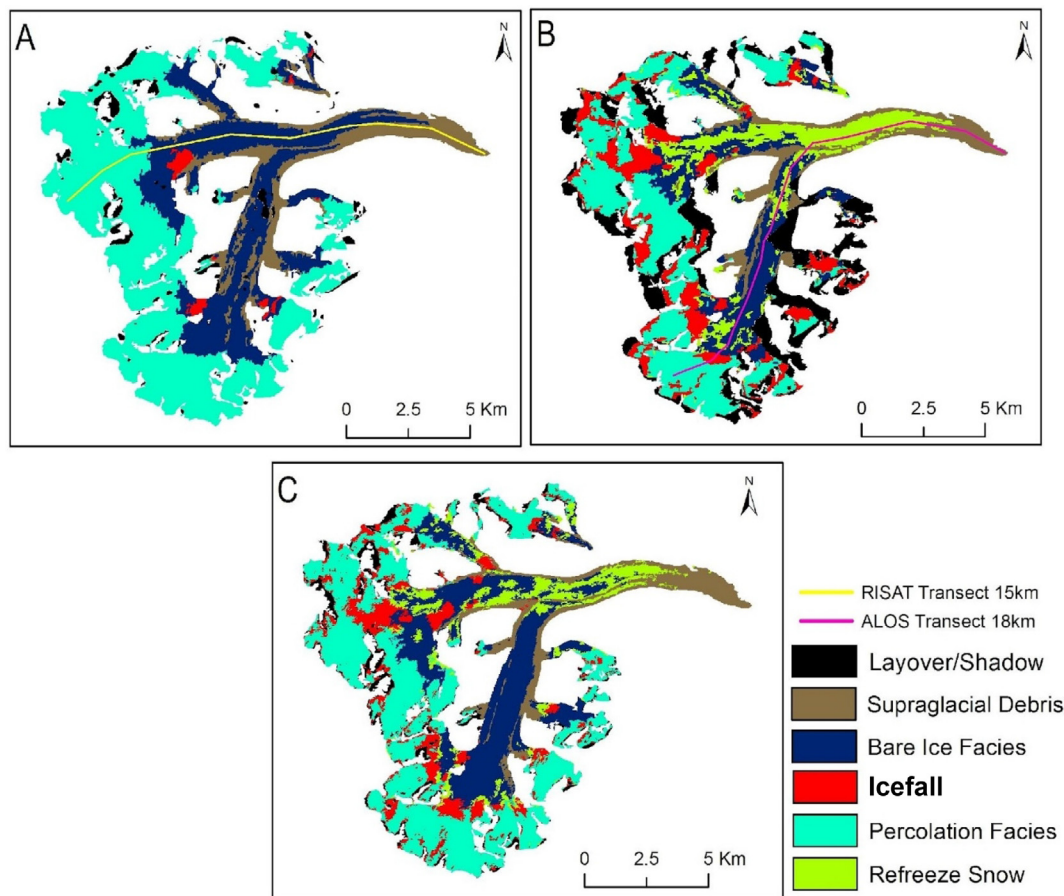
Fig. 8. Classification Results **A)** Multi-Temporal RISAT-1 dataset **B)** ALOS/PALSAR (12-Apr-2011) **C)** RADARSAT-2 dataset (27-Jan-2014).

phase values were finally used to derive horizontal displacement. We chose SRTM DEM for the removal of topographic phase and then for further processing in phase unwrapping and geocoding. Vertical accuracy of SRTM DEM is high and error contribution in glaciological application is less compared to ASTER DEM (Racoviteanu et al., 2007). Patterns of glacier flow in the direction of radar i.e., line of sight (LOS) velocity are shown as differential fringes (Fig. 13A and 13B) in the interferogram for March and May for 1996. Images were cropped to show the detailed flow pattern. The area of the glacier affected by layover and shadow distortions was removed, as the velocity values in these regions were unrealistic. For the month of March, most part of the glacier remained decorrelated likely due to snowfall between the two acquisitions. In the month of May whole of the glacier shows good correlation except the lower ablation area probably due to the melting of snow in lower reaches. Higher density of fringes in May indicate higher flow rates. The velocity fields in cm/day are shown for 28–29 March 1996 and 2–3 May 1996 (Fig. 13 C and 13D). It was found that the mean surface velocity of the glacier is around 62.05 m/year in March, which increased to 81.03 m/year in the month of May 1996. The obtained results show that glacial flow varies with season most likely due to the excessive heat in the

month of May which produces excessive melt water at the base causing enhanced basal flow. Low flow rates are seen near the snout of the glacier (in accordance to the literature, e.g., Sahu & Gupta, 2019; Patel et al., 2021). Higher values of glacier flow are seen in the two northern branches of the glacier. The velocity fields indicate that glacier flow is not uniform it varies through and across it, so there is need to study displacement with variation in slope and aspect. The Fig. 14A and 14B shows the variation in mean displacement during March and May with respect to aspect, highest flow rates in southern aspects. The variation in the glacier velocity patterns with respect to slope are shown in the Fig. 15A and 15B. The 2–3 May 1996 pair shows expected increase in ice velocity with increase in slope, whereas, 28–29 March 1996 pair shows slight decrease in ice velocity between 0 and 30° slope and expected increase in velocity beyond 30°.

4.6. Glacier velocity using feature tracking

The results from the Figs. 16 and 17 (Profile 1) indicate that there has been a decrease in rate of glacier flow over the period (2000–14). The ITS_Live data products (Gardner et al., 2019) based velocity for this glacier are
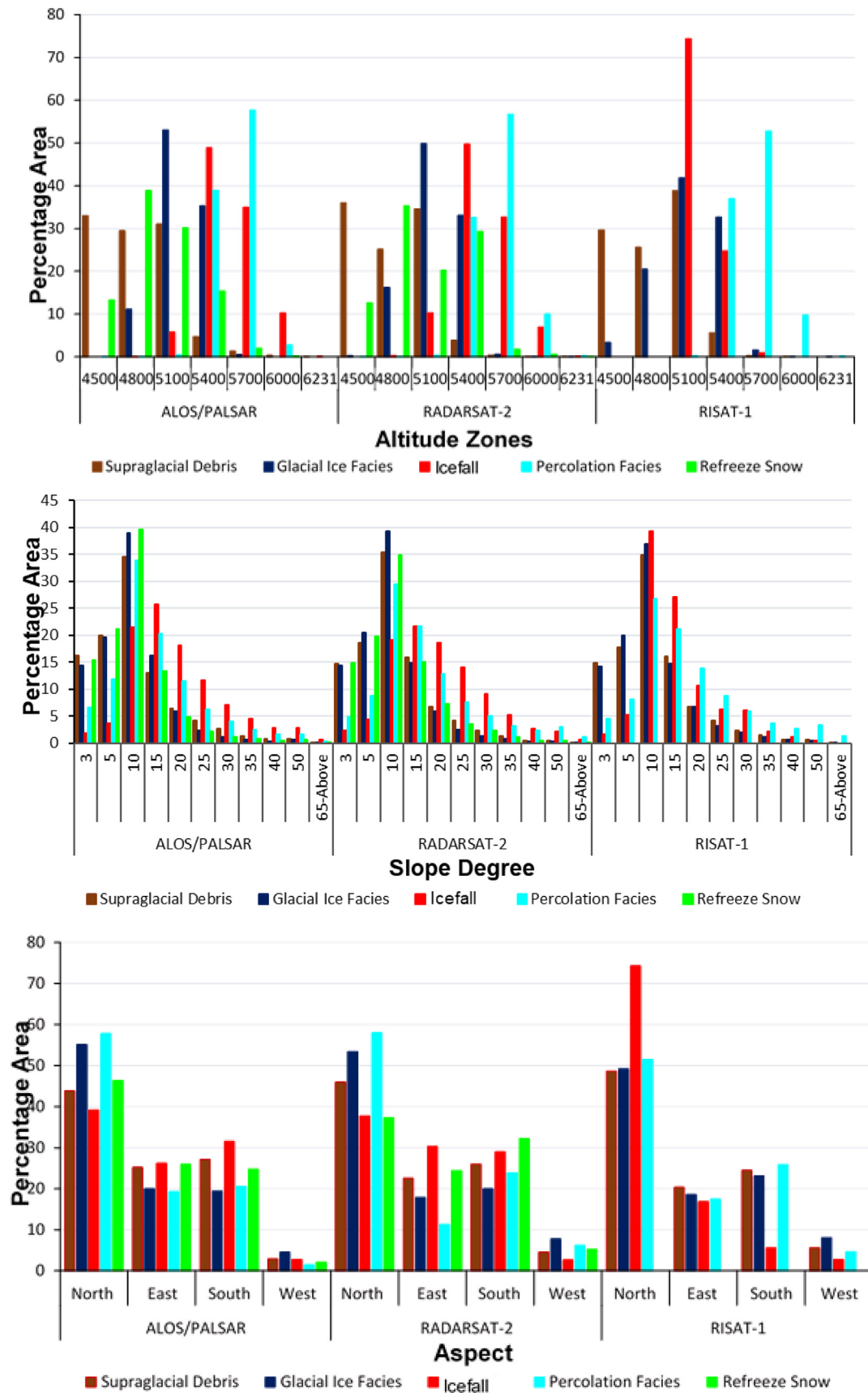
Fig. 9. Percentage area of classified glacier radar zones in various A) Elevation zones B) Slopes C) Aspect.
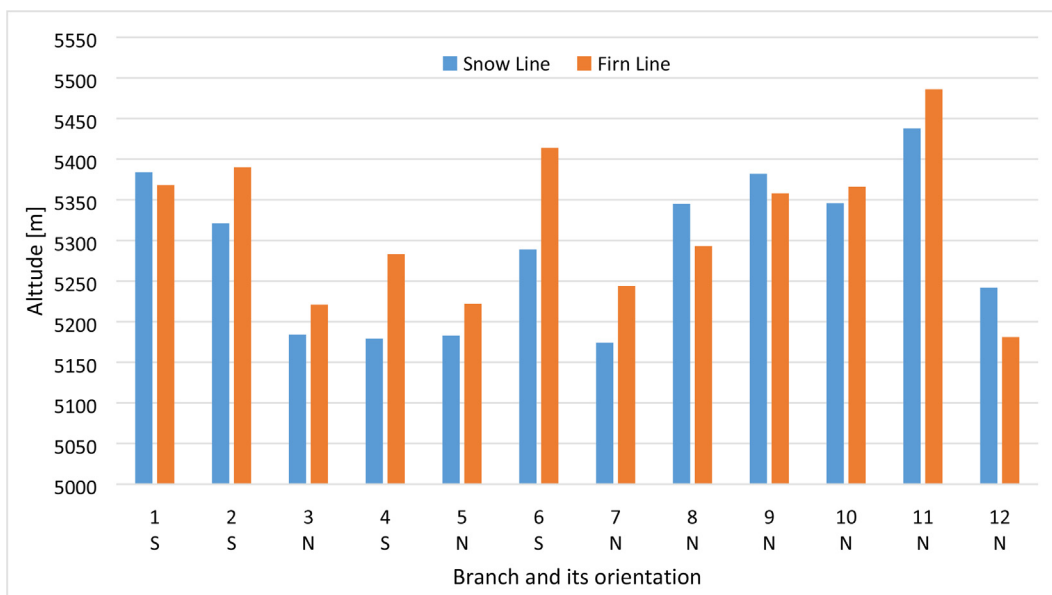
Fig. 10. Snow line and firn line altitude in the different branches of the glacier estimated from the wintertime image of RADARSAT-2 (27-Jan-2014) and SRTM-DEM.
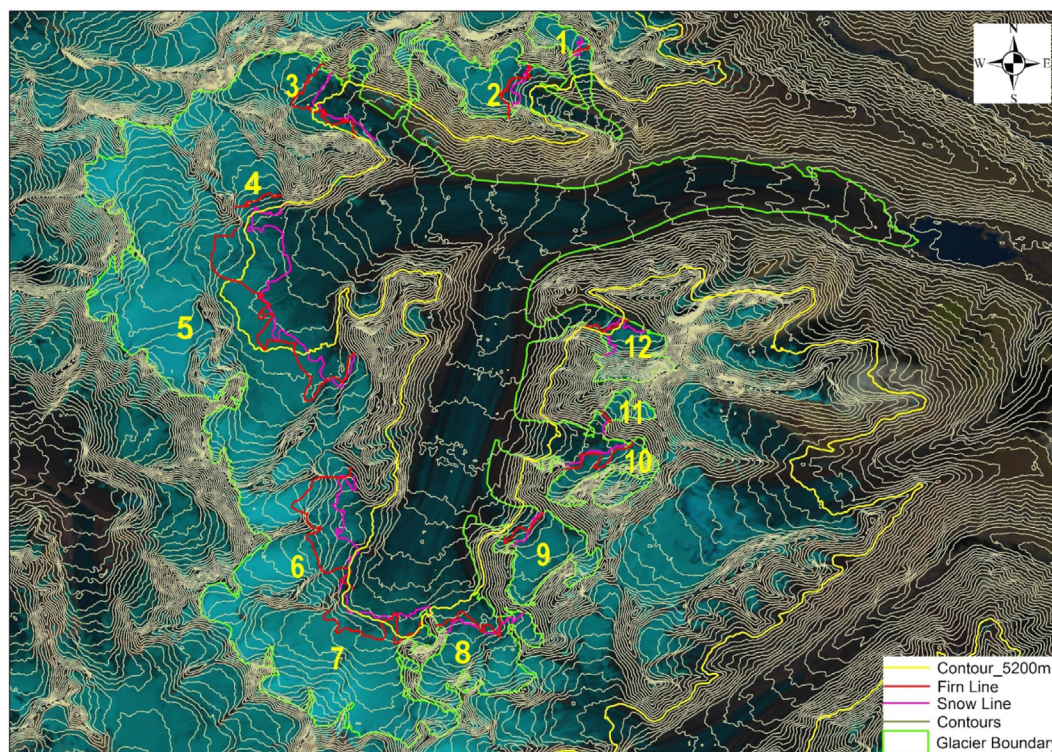

Fig. 11. Snow line and firn line overlapped on the contour lines. The yellow line is 5200 m contour line which is used as a reference, the contour interval is 40 m. Background is the Landsat-8 image 30-September-2015.

given in Table 3b and Fig. S8a and S8b of the supplementary data.

(See Fig. 18).

The mean glacier velocity reduced to 19.3 m/year in 2014–2020, as compared to higher mean velocity of 44.26 m/year estimated for 1999–2003 (Table 3a),

indicating loss of ice (Dehecq et al., 2019). It should be noted that the mean velocity given in Table 3aa refers to mean velocity over entire glacier. The analysis of glacier velocity over point based profiles (see Figure S7 of the supplementary data) velocity along two main branches revealed higher mean velocity (see Fig. S8a and S8b of
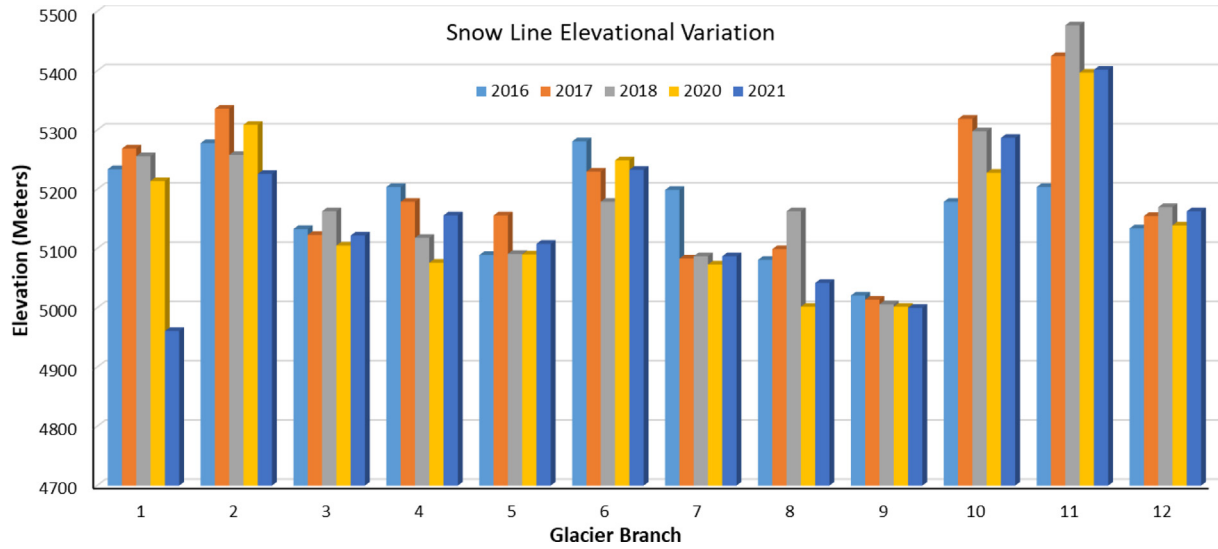
Fig. 12. Snow line elevation variations for various branches of Smudra Tapu glacier as derived from time-series of Sentinel-1 SAR data.
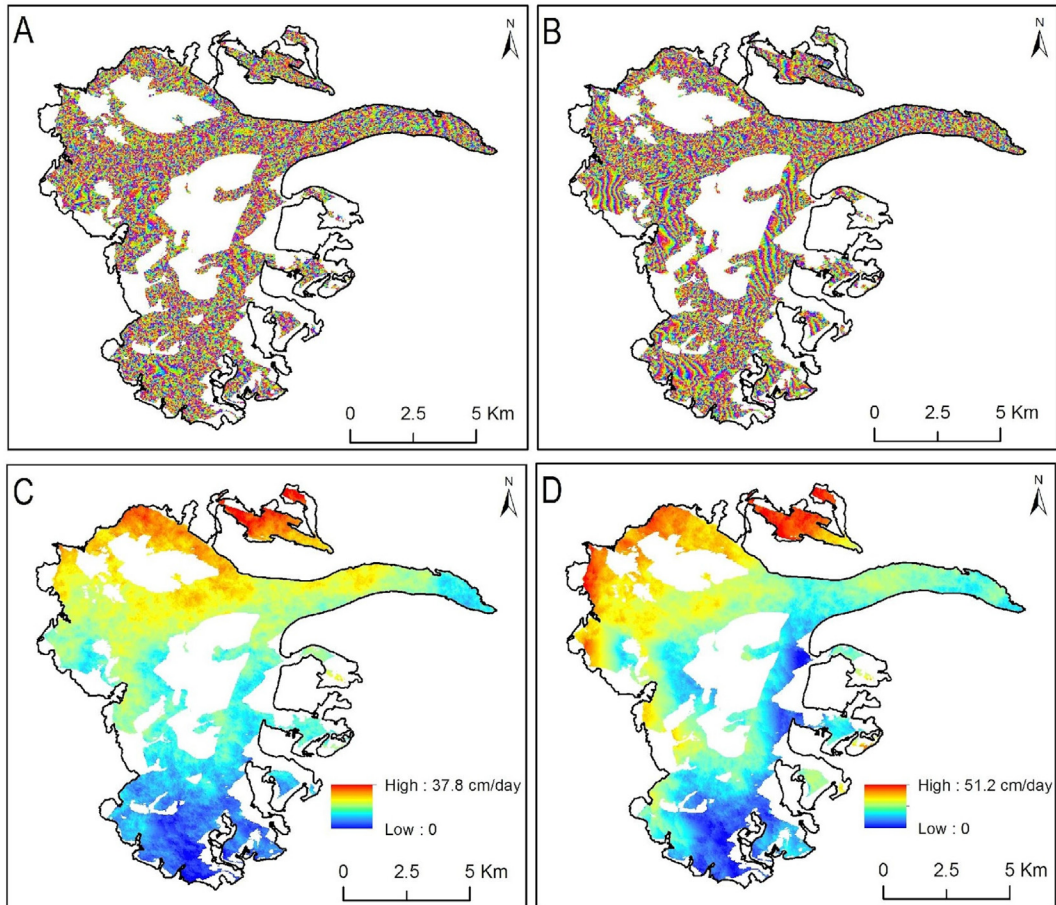

Fig. 13. A) Interferogram for 28th-29th-March-1996B) Interferogram for 2nd-3rd-May-1996C) Displacement map for 28th-29th-March-1996 D) Displacement map for 2nd-3rd-May-1996.

the supplementary data) for both Its_Live at 240 m resolution and our study at 15–30 m resolution. The mean glacier velocity for both point based profiles reduced to 49.5 m/year in 2014–2020, as compared to higher mean velocity of 67.67 m/year estimated for 1999–2003 (Table 3b). In both the cases, higher velocity were estimated for the years
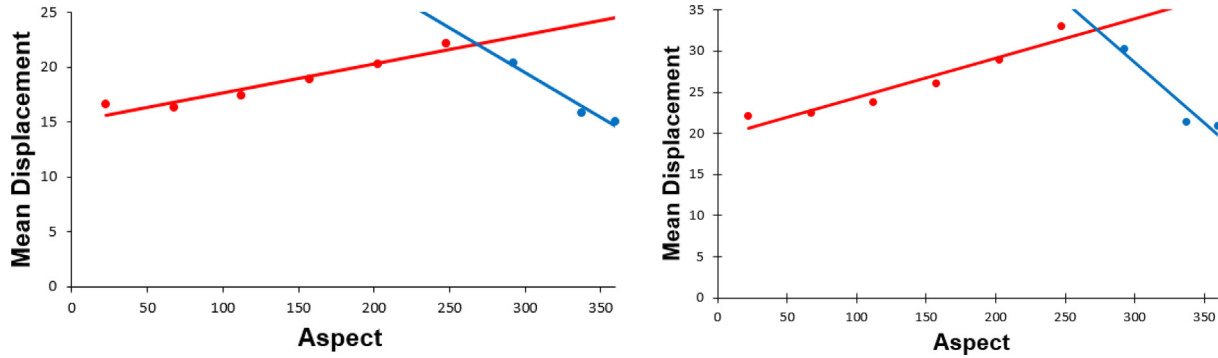
Fig. 14. Mean displacement A) 28th-29th-March-1996B) 2nd-3rd-May-1996 w.r.t. aspect.
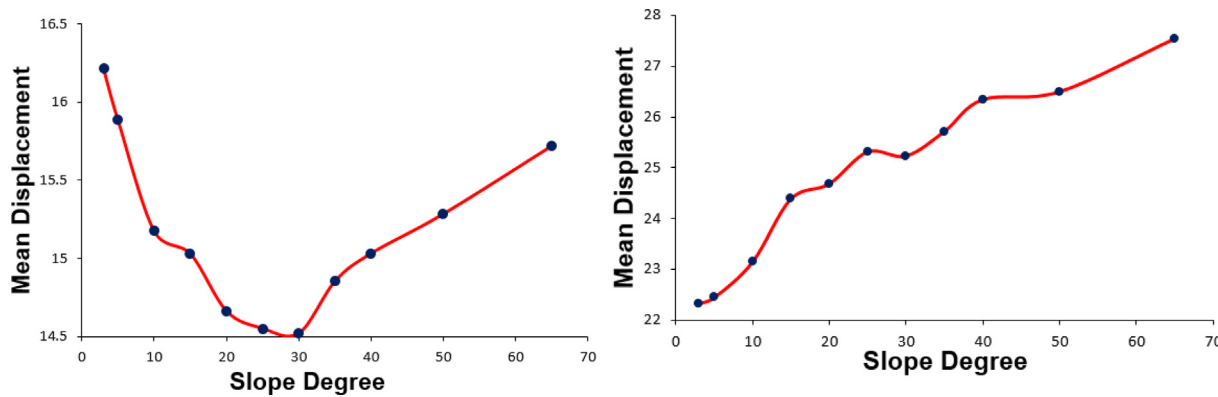

Fig. 15. Mean displacement A) 28th-29th-March-1996B) 2nd-3rd-May-1996 w.r.t. slope.

2001 and less velocity was observed for the year 1999, indicating good snowfall in the year 2000–2001 and less snow or more –ve mass balance in the year 1998–99.

The results in the Table 3a and Table 3b are the estimated values of per year glacier velocity in different seasons, and annual time scale over a certain time-period. The feature tracking velocity estimates are correct only in the snow free regions of the image, as the snow free regions vary from image to image. Table 3 considers the lower ablation area which appears like the tongue of the glacier. Most of the used optical image pairs have a time difference of about a year so these maps represent the annual glacier flow. The annual glacier surface velocity of Samudra Tapu was estimated from the year 1999 to 2020. It was noted that the annual glacier surface velocity is decreasing with time. The decrease in glacier surface movement with time depicted the loss of ice mass in the glacier (Dehecq et al., 2019). The results obtained from SAR interferometry of ERS-1/2 Tandem datasets are representation of glacier flow for one day time period. TanDEM-X glacier flow estimates represent the end of ablation season. RISAT-1 velocity estimates represent the whole ablation season.

The satellite based Samudra Tapu glacier snout retreat is given in the Table 4. The snout position was estimated using the satellite imagery, the Corona image of the year 1973 was taken as base and for the rest (1979–89; 1989–2000; 2000–2015; and 2014–2021) Landsat archived

imageries were used. It was observed that the front of the glacier retreated maximum during the period from 2000 to 2015 with a magnitude of 452 m at the rate of 30.28 m/year. The minimum retreat of 96.47 m was observed for the period of 1973–1979. The total retreat of Smudra Tapu glacier snout is estimated as ~ 1300 m during 1973–2021 time, with a mean retreat rate of 27 m per year.

4.7. Rate of flow for glacier facies

We mapped glacier facies that define the accumulation and ablation zones and estimated glacier flow. We can also determine the rate of transport of ice from accumulation to ablation region. From the derived glacier facies, we can say that percolation facies form the accumulation area and rest is ablation zone. We have used the classified maps and InSAR velocity patterns, which represent the ice flow for whole of the glacier to determine the rate of ice flow from accumulation to ablation region. For this, we have used RISAT-1 classified map as an input because icefalls in the accumulation zone and percolation facies are classified as one class that collectively form the accumulation area. We have used March 1996 DInSAR velocity estimates that were closer to the annual glacier flow. The glacier velocity in units meter per day for various glacier facies are given in Table 5. Maximum flow rates of more than 37.8 cm/day
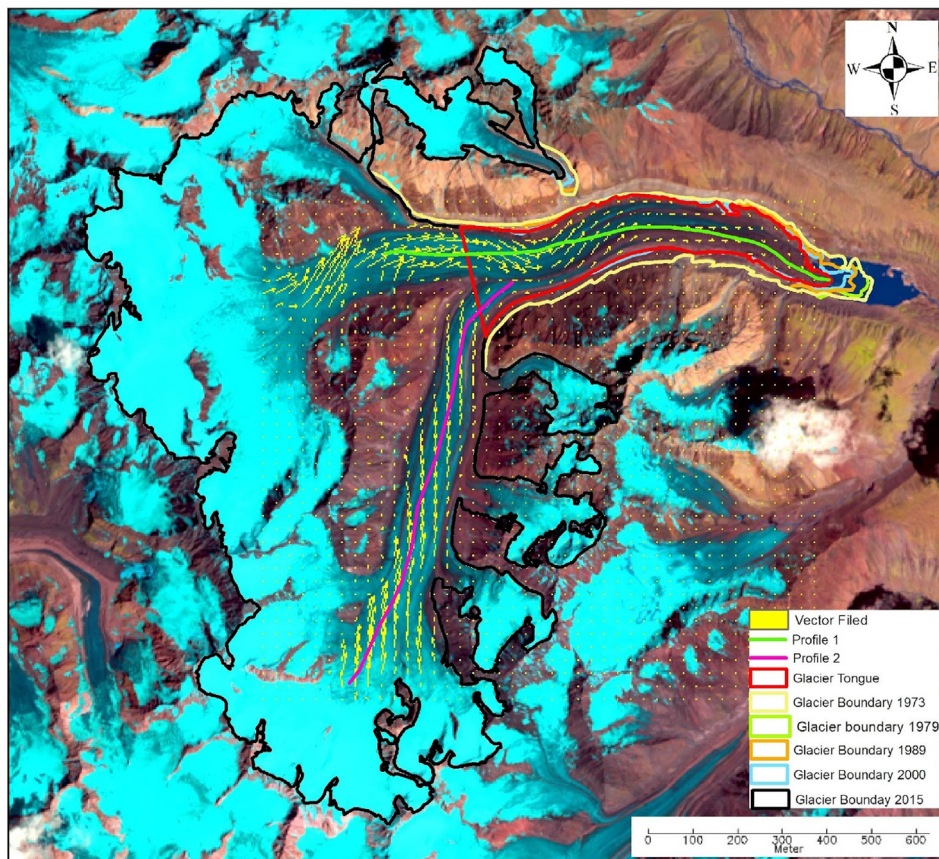
Fig. 16. Vector field overlaid on Samudra Tapu glacier Landsat FCC (30 Aug 2015). The profiles are the vector lines drawn along centre of the glacier; Profile 1 is drawn along main branch of the glacier (East Aspect); Profile 2 is drawn along centre of the 2nd main branch of the glacier (North-East aspect). The glacier snout as derived from various RS data sources from 1973 to 2015 is overlaid as vector files on Landsat FCC.

Table 3a
Estimated average velocity values for the Samudra Tapu glacier.

Satellite	Time Interval (Days)	Selected Image Pair	Mean Velocity m year-1
ERS 1/2 Tandem	1	28/03/1996 – 29/03/1996	62.05
ERS 1/2 Tandem	1	02/05/1996 – 03/05/1996	81.03
Landsat-7 ETM	415	09/07/1999 – 28/08/2000	43.44
Landsat-7 ETM	304	28/08/2000 – 28/06/2001	44.17
Landsat-7 ETM	400	28/06/2001 – 02/08/2002	44.17
IRS-1C	322	15/08/2002 – 03/07/2003	45.26
IRS-1D-1C	360	01/07/2006 – 26/06/2007	33.95
RISAT-1	200	15/04/2013 – 01/11/2013	60.96
TanDEM-X	33	25/09/2013 – 28/10/2013	69.72
Landsat-8 OLI	384	23/07/2013 – 11/08/2014	20.23
Landsat-8 OLI	384	11/08/2014 – 30/08/2015	19.44
Landsat-8 OLI	351	30/08/2015 –16/08/2016	19.46
Landsat-8 OLI	384	16/08/2016 –04/09/2017	17.97
Landsat-8 OLI	384	22/08/2018 – 10/09/2019	21.11
Landsat-8 OLI	375	10/09/2019 –12/09/2020	17.61

were seen in percolation facies i.e. the accumulation zone, but the value of mean displacement is minimum of about 10 cm/day in this zone. This represent the ice velocity from the region of accumulation into the ablation region. There is huge variation in the flow rates of percolation facies or accumulation zone because of the distribution of this class in high and low sloppy terrain. Lower ablation zone shows relatively less glacier ice velocity.

5. Discussions

5.1. Mapping of glacier facies

RISAT-1 SAR images from middle and end of ablation season along with winter were used to locate glacier facies. Using multi-temporal RISAT-1 images, glacier facies were identified as percolation facies, bare ice facies and supra-

Table 3b
Estimated average velocity values for the Samudra Tapu glacier using ITS_Live data.

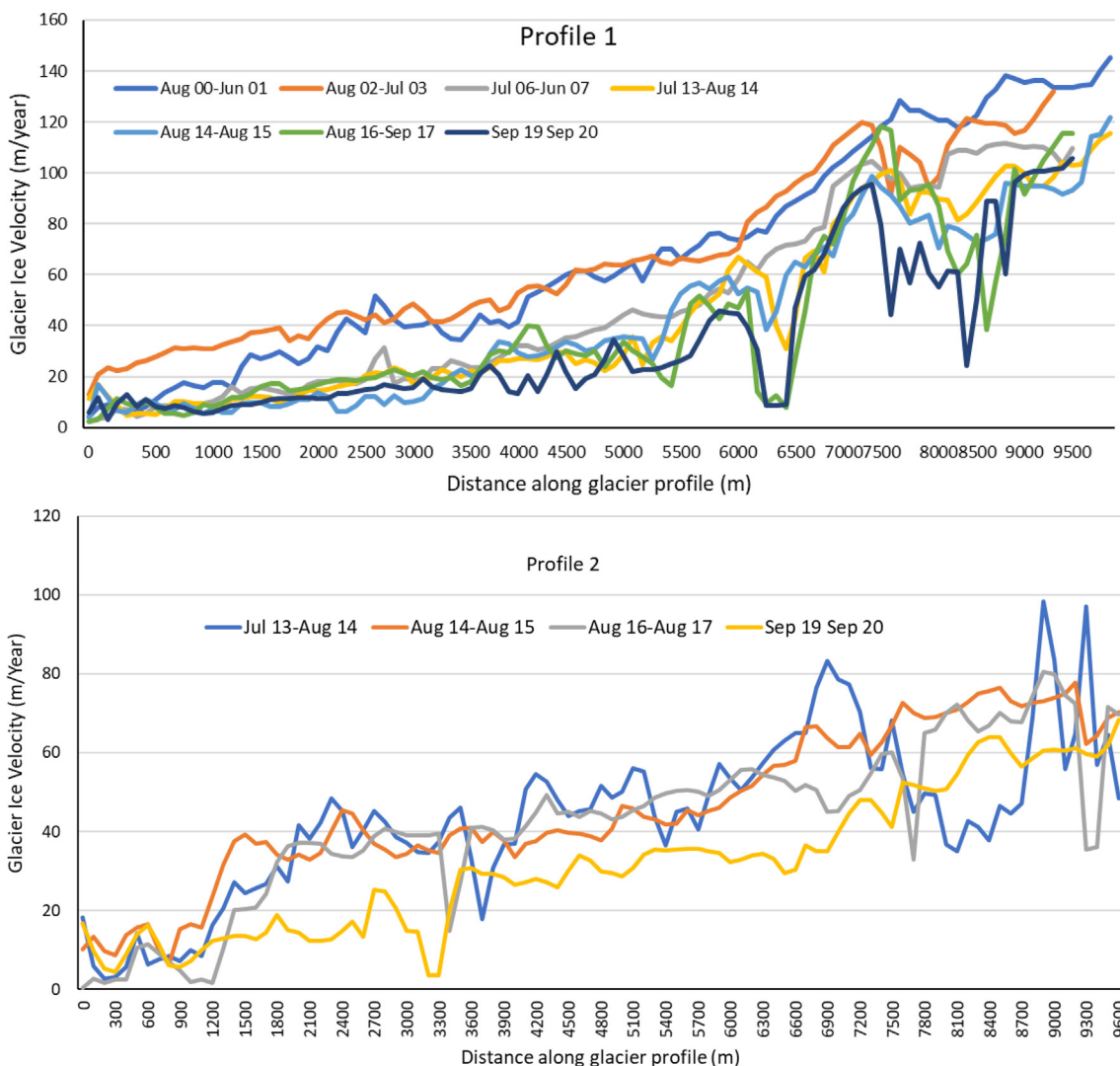| Data source	Year	Mean (m/year)	Std Dev (m/year)	Mean (Profile 1) (m/year)	Mean (Profile 2) (m/year)
ITS_Live_240m	1989	36.42	34.99	90.45	39.44
	1999	27.62	34.29	83.59	45.07
	2001	32.30	37.82	96.89	57.21
	2003	27.35	33.19	81.46	41.82
	2009	18.69	27.55	66.44	29.03
	2015	25.60	32.14	76.73	39.03
	2018	25.52	30.47	71.09	38.25

Fig. 17. Glacier velocity profiles along the Samudra Tapu glacier in different years as derived from Landsat and IRS datasets using feature-tracking method.

glacial debris. Using polarimetric decompositions of fully polarimetric L- band ALOS/PALSAR and C-band RADARSAT-2 datasets, the scattering matrix can be decomposed into different types of scatters i.e. volume, surface and double bounce scattering and the secondary decomposition parameters such as entropy, α and anisotropy to map different glacier facies. Using fully polarimetric datasets icefalls and refreeze snow were identified which

were not visible in the multi-temporal SAR image thereby surplus glacier facies can be identified using polarimetric decompositions. The identified glacier facies can also be seen in the field photographs (Fig. 2) taken during the field visit (1st week of October 2013), which provide the validation of the obtained results. The classification of ALOS/ PALSAR dataset show more coverage of refreeze snow and icefalls than RADARSAT-2 data. It could be because
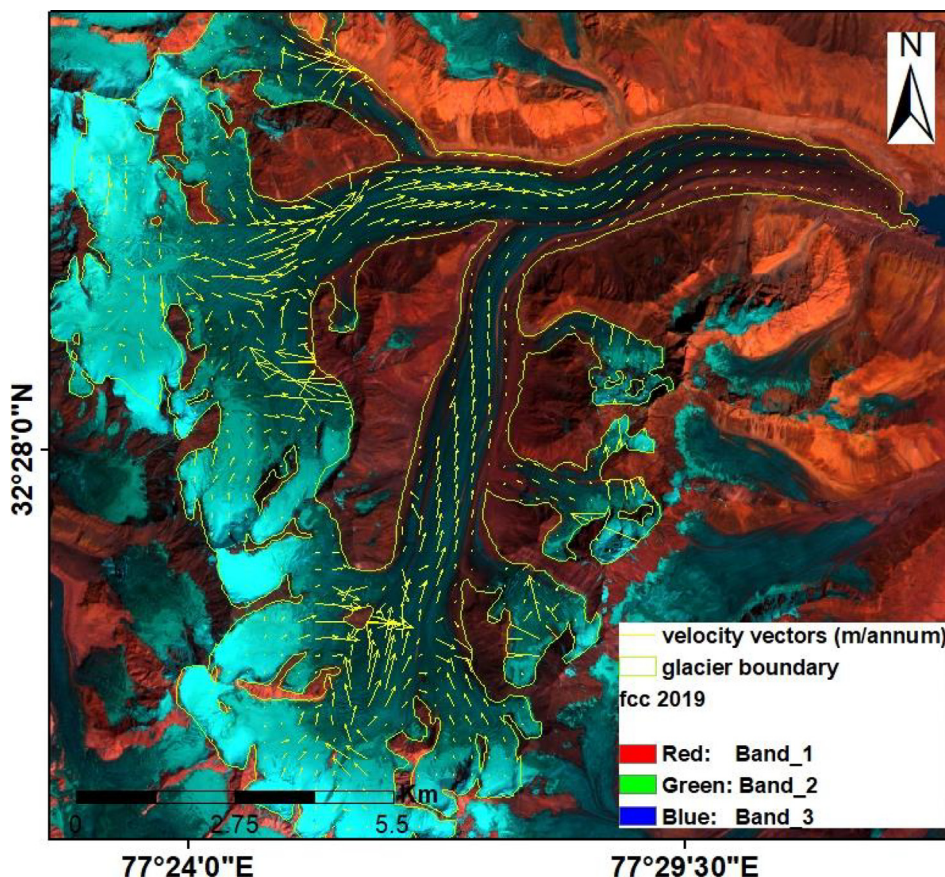
Fig. 18. Vector field overlaid on Samudra Tapu glacier 2019 Sentinel-2 FCC.

Table 4
Retreat of Samudra Tapu glacier.

Time Period	Snout Retreat (m)	Snout Retreat Rate (m per year)
1973–1979	96.47	16.07
1979–1989	375.49	37.54
1989–2000	236.47	21.49
2000–2015	451.92	30.28
2014–2021	150.20	21.42

Table 5
Rate of flow of glacier facies using InSAR velocity pattern for March 1996.

Class	Maximum Displacement (cm)	Mean Displacement (cm)	Standard Deviation (cm)
Supraglacial debris	33.4	14.0	7.6
Ice facies	34.4	13.5	9.0
Icefalls	29.1	13.9	8.3
Percolation facies	37.8	10.0	9.7

season, refreeze snow would disappear because it would have melted away in the summer. The lowest altitude of refreeze snow marks the snow line altitude before winter season. Object oriented classification using the multi-resolution segmentation was used for mapping of glacier facies. Segmentation in case of ALOS/PALSAR and RADARSAT-2 was done using eight layers but only the layers, which had the maximum class separability in the feature space, were used for nearest neighbour classification algorithm. In RISAT-1, all the classes were easily separable but in case of ALOS/PALSAR and RADARSAT-2 datasets, class refreeze snow had minimum separability with glacial ice. Spatial profile for RADARSAT-2 backscatter coefficient in various polarizations did not show much variations throughout the glacier as the C-band data was not able to fully penetrate the seasonal dry snow. However, we were able to identify and map various glacier facies using the target decompositions. Most of the refreeze snow was found at higher altitudes especially in the southern aspects that receive maximum sunlight. Therefore, snow melts even at higher reaches of the glacier. The multi-temporal approach uses end of ablation season image thus snow line was detected as the boundary between percolation and ice facies. The firn line was detected using classified results of fully polarimetric RADARSAT-2 winter image. The two key factors which are responsible for

of the more penetration capabilities of the L-band ALOS/PALSAR data than the C-band RADARSAT-2 dataset. The derived glacial facies were found to have seasonal effect. If we use the fully polarimetric image of end ablation

the variation of snow and firn line altitude are slope and aspect. The southern aspects receive more sunshine thus snow and firn line shrink to higher altitudes. Another key factor is the slope, if slope is gentle, there is more accumulation of snow thus snow and firn are found at the lower altitudes in the case of sloppy terrain. According to the study by (Huang et al., 2013) at the end of summer, snow line is at a higher altitude than firn line that depicts negative mass balance. This may be applicable to our study but here we have to assume that 18-August-2013 RISAT-1 dataset is the end of summer condition and the snow line will not shift up further. If the ablation season extends further the snow line will shift to higher altitudes depicting much more negative mass balance for the year. The degree of slope and its orientation are important factor responsible for the altitude of snow line and firn line.

5.2. Glacier velocity estimation

SAR interferometric approach has been used to estimate glacier velocity using ERS-1/2 datasets. Since InSAR based deformations are only sensitive to radar Line Of Sight (LOS) thus the East-West component was noticed. One of the main branch of the Samudra Tapu glacier is oriented in the East-West direction flowing from West to East, and other branch from South-North, thus InSAR technique is suitable for this West to East branch. Highest mean value of displacement was found in the southern aspects whereas the lowest displacement rates were found in the northern aspect. This difference arises because the southern aspects are most sun illuminated whereas the northern aspects are least exposed to the sunlight. The highest value of the displacement was found in the south-west aspect and start to dip thereafter. The point of intersection of the lines signifies the point at angle of 260° after which the displacement values start to dip. There is variation in flow pattern with respect to slope in March and May. For the month of March initially there is a dip in the values of mean displacement with increasing slope but after slope reaches to 30°, an increasing pattern in mean displacement was observed. A continuous increasing pattern of displacement with respect to slope was noted for the month of May. This variation in the flow pattern is due to the variation in temperature in these months. The slope between 5°-30° were found at the higher reaches of the glacier in the month of March. The temperature remain reasonably below the freezing point so there is not enough melt water at the base limiting the basal flow. There is initial dip in the curve, thereafter the glacier flow increases in high sloppy areas due to the profound effect of slope. Feature tracking technique was applied on SAR and optical image pairs which represented different seasons over time. The obtained results indicated that glacier flow varies with seasons of the year and are comparable with the published work on Samudra Tapu glacier (Sahu and Gupta, 2019; Patel et al., 2021). However, the GNSS based glacier velocity of Patel et al 2021 showed higher mean velocity (64.3 m/

year for 2017–18 season), which is higher than our estimates. This can be due fact that we have taken mean glacier velocity for the entire glacier, whereas the GNSS survey was done along two main branches of this glacier. When compared with the limited points based profiles along two main branches of the glacier (see section 4.7), our results (with a mean of 49.64 m/year for 2014–2020) are slightly lower comparable with the results of GNSS based survey, and Its_Live data (with a mean of 53.42 m/year for 2009–2018 and 67 m/year for 1989–2003). Spatial glacier velocity as derived from our study and ITS_Live data are also matching, with our results showing much finer details as due to higher spatial resolution.

Overall, there has been a small decrease in the glacier flow over a time-period from 1999 to 2020. According to the study by (Berthier et al., 2007) most of the glaciers in the western Himalayas are experiencing loss in mass, as the depth of the glacier is directly proportional to its velocity (Mcnabb et al., 2012). This loss of mass of glacial ice may have led to decrease in its flow over the years.

6. Conclusions

Different glacier facies exhibit different scattering mechanisms and show variation in the amount of radar backscatter in different seasons. Thus glacier facies can be mapped using multi-temporal SAR datasets and polarimetric decompositions of fully polarimetric SAR data.

The ALOS/PALSAR datasets used in this study had geometric distortions in huge amount of area about 19.20 km^2 in the form of layover and shadow this was because of the low incidence angle at which the scene is acquired which does not work well in high relief areas such as these. Ideally for identifying the glacier facies we require fully polarimetric SAR datasets at high incidence angle for winter season, so that end of summer situation is preserved under the dry snow. Alternatively, fully polarimetric SAR data for the end of ablation season is optimal for identification of glacier facies, and it can be explored in future studies. Our glacier facies mapping results indicate that various branches of Samudra Tapu glacier have a minimum and maximum ELA ranges from 5001 to 5477 m, mean ELA of 5173 and mean standard deviation of 109 m, during the 2016–2021 time-period. In future studies time-series of multi-frequency SAR data from C-, S- and L-band of RISAT-1A, NISAR and ALOS-2 satellites can provide an improved discrimination of snow/firn/equilibrium line altitude using SAR data. This can enable all weather, all season control on glacier mass balance indicators, which can be derived from remote sensing.

In this study, feature-tracking technique was used to validate the DInSAR derived velocity results, and generate long time series of glacier velocity at high spatial resolution. Our results we can conclude that glacier flow varies with season as well as annually, depending on prevailing melting and overall mass balance status in a year. More snowfall during winter and more melting during summer

can induce higher velocity on annual as well spring-summer time. Our study concludes there has been reduction of ∼ 10–15 m/year in glacier velocity along with a mean snout retreat of 25.85 m/y for the Samudra Tapu glacier during the last 20 years. Furthermore, this reduction in glacier ice velocity is directly related to its loss of mass, indicating more negative mass balance in the recent years. The DInSAR velocity estimates were representation of few days, whereas the feature tracking results were representing seasonal or annual glacier flow so these results. In future, attempt will be made to explore limited 6-day interval Sentinel-1 data (Mahagaonkar et al., 2019), ALOS-PALSAR 1,2 data at 14 day interval (Thakur et al., 2018) and upcoming NISAR data at 12 day interval to estimate the fortnightly to seasonal glacier velocity.

Declaration of Competing Interest

The authors declare that they have no known competing financial interests or personal relationships that could have appeared to influence the work reported in this paper.

Acknowledgements

Appendix A. Supplementary material

Supplementary data to this article can be found online at https://doi.org/10.1016/j.asr.2022.10.030.

References

Abe, T., Yamaguchi, Y., Sengoku, M., 1990. Experimental study of microwave transmission in snowpack. IEEE Trans. Geosci. Remote Sens. 28 (5), 915–921.

Adam, S., Pietroniro, A., Brugman, M.M., 1997. Glacier snow line mapping using ERS-1 SAR imagery. Remote Sens. Environ. 61 (1), 46–54. https://doi.org/10.1016/S0034-4257(96)00239-8.

Azam, M.F., 2021. Need of integrated monitoring on reference glacier catchments for future water security in Himalaya. Water Security 14. https://doi.org/10.1016/j.wasec.2021.100098 100098.

Benson, C.S., 1961. Stratigraphic studies in the snow and firn of the Greenland ice sheet. Folia Geogr. Dan. 9, 13–37.

Benson, C., Motyka, R., McNutt, S., Lüthi, M., Truffer, M., 2007. Glacier-volcano interactions in the North Crater of Mt Wrangell, Alaska. Ann. Glaciol. 45, 48–57. https://doi.org/10.3189/172756407782282462.

Benson, C. S. (2001). The History of the Glacier Facies Concept. AGU Fall Meeting Abstracts, AA, University of Alaska, Fairbanks, Geophysical Institute), December 2001, IP12B-06. https://ui.adsabs.harvard.edu/abs/2001AGUFMIP12B..06B.

Berthier, E., Arnaud, Y., Kumar, R., Ahmad, S., Wagnon, P., Chevallier, P., 2007. Remote sensing estimates of glacier mass balances in the Himachal Pradesh (Western Himalaya, India). Remote Sens. Environ. 108, 327–338. https://doi.org/10.1016/j.rse.2006.11.017.

Bhardwaj, A., Joshi, P. K., Snehmani, Sam, L., Singh, M. K., Singh, S., & Kumar, R. (2015). Applicability of Landsat 8 data for characterizing glacier facies and supraglacial debris. *International Journal of Applied Earth Observation and Geoinformation*, 38(0), 51–64. http://doi.org/http://dx.doi.org/10.1016/j.jag.2014.12.011.

Bisset, R.R., Dehecq, A., Goldberg, D.N., Huss, M., Bingham, R.G., Gourmelen, N., 2020. Reversed surface-mass-balance gradients on Himalayan debris-covered glaciers inferred from remote sensing. Remote Sensing 12 (10), 1563.

Bolch, T., Kulkarni, A., Kääb, A., Huggel, C., Paul, F., Cogley, J.G., Frey, H., Kargel, J.S., Fujita, K., Scheel, M., Bajracharya, S., Stoffel, M., 2012. The state and fate of Himalayan glaciers. Science 336, 310–314. https://doi.org/10.1126/science.1215828.

Cloude, S.R., Pottier, E., 1997. An Entropy Based Classification Scheme for Land Applications of Polarimetric SAR. IEEE Trans. Geosci. Remote Sens. 35 (1), 68–78. https://doi.org/10.1109/36.551935.

Collier, E., Maussion, F., Nicholson, L.I., Mölg, T., Immerzeel, W.W., Bush, A.B.G., 2015. Impact of debris cover on glacier ablation and atmosphere–glacier feedbacks in the Karakoram. The Cryosphere 9, 1617–1632. https://doi.org/10.5194/tc-9-1617-2015.

Definiens Developer XD 2.0.4 (2012). *Reference Book.* Definiens AG, Bernhard-Wicki-Straße 5, 80636 München, Germany, 436 pages.

Dehecq, A., Gourmelen, N., Gardner, A.S., Brun, F., Goldberg, D., Nienow, P.W., Berthier, E., Vincent, C., Wagnon, P., Trouvé, E., 2019. Twenty-first century glacier slowdown driven by mass loss in High Mountain Asia. Nat. Geosci. 12, 22–27.

Dhar, S., Kulkarni, A.V., Rathore, B.P., Kalia, R., 2010. Reconstruction of the moraine dammed lake, based on field evidences and paleo-history, Samudra Tapu Glacier, Chandra Basin, Himachal Pradesh. Indian Soc. Remote Sens. 38, 133–141. https://doi.org/10.1007/s12524-010-0004-z.

Dixit, A., Sahany, S., Kulkarni, A.V., 2021. Glacial changes over the Himalayan Beas basin under global warming. J. Environ. Manage. 295. https://doi.org/10.1016/j.jenvman.2021.113101 113101.

Eriksson, M., Jianchu, X., Shrestha, A.B., Vaidya, R., Nepal, S., and Sandstrom, K. (2009). *The changing Himalayas - Impact of climate change on water resources and livelihoods in the Greater Himalayas. International Centre for Integrated Mountain Development (ICIMOD).* (Kathmandu, Nepal). 25 pages.

Evans, A.N., 2000. Glacier surface motion computation from digital image sequences. IEEE Trans. Geosci. Remote Sens. 38 (2), 1064–1072.

Frey, H., Paul, F., Strozzi, T., 2012. Compilation of a glacier inventory for the western Himalayas from satellite data: methods, challenges, and results. Remote Sens. Environ. 124, 832–843. https://doi.org/10.1016/j.rse.2012.06.020.

Gaddam, V.K., Boddapati, R., Kumar, T., Kulkarni, A.V., Bjornsson, H., 2022. Application of "OTSU"—an image segmentation method for differentiation of snow and ice regions of glaciers and assessment of mass budget in Chandra basin, Western Himalaya using Remote Sensing and GIS techniques. Environ. Monit. Assess. 194 (5), 1–18.

Gardner, A. S., Fahnestock, M. A. and Scambos, T. A. (2019). [accessed in May 2022]: MEaSUREs ITS_LIVE Landsat Image-Pair Glacier and Ice Sheet Surface Velocities: Version 1, https://doi.org/10.5067/IMR9D3PEI28U.

Giles, B., Massom, R., Warner, R.C., 2009. A method for sub-pixel scale feature-tracking using Radarsat images applied to the Mertz Glacier Tongue, East Antarctica. *Remote Sens. Environ.* 113 (8), 1691–1699. https://doi.org/10.1016/j.rse.2009.03.015.

Gourmelen, N., Kim, S. W., Shepherd, a., Park, J. W., Sundal, a. V., Björnsson, H., & Pálsson, F. (2011). Ice velocity determined using conventional and multiple-aperture InSAR. *Earth and Planetary Science Letters*, 307(1-2), 156–160. http://doi.org/10.1016/j.epsl.2011.04.026.

Harrison, S., Kargel, J.S., Huggel, C., Reynolds, J., Shugar, D.H., Betts, R.A., Vilímek, V., 2018. Climate change and the global pattern of moraine-dammed glacial lake outburst floods. The Cryosphere 12 (4), 1195–1209.

Hu, J., Li, Z., Li, J., Zhang, L., Ding, X., Zhu, J., Sun, Q., 2014. 3-D movement mapping of the alpine glacier in Qinghai-Tibetan Plateau by integrating D-InSAR, MAI and Offset-Tracking : case study of the Dongkemadi Glacier. Global Planet. Change 118, 62–68. https://doi.org/10.1016/j.gloplacha.2014.04.002.

Huang, L., Li, Z., 2011. Comparison of SAR and optical data in deriving glacier velocity with feature tracking. Int. J. Remote Sens. 32 (10), 2681–2698. https://doi.org/10.1080/01431161003720395.

Huang, L., Li, Z., Tian, B.-S., Chen, Q., Liu, J.-L., Zhang, R., 2011. Classification and snow line detection for glacial areas using the polarimetric SAR image. Remote Sens. Environ. 115 (7), 1721–1732. https://doi.org/10.1016/j.rse.2011.03.004.

Huang, L., Li, Z., Tian, B., Chen, Q., Zhou, J., 2013. Monitoring glacier zones and snow / firn line changes in the Qinghai – Tibetan Plateau using C-band SAR imagery. Remote Sens. Environ. 137, 17–30. https://doi.org/10.1016/j.rse.2013.05.016.

Jaenicke, J., Mayer, C., Scharrer, K., Munzer, U., Gudmundsson, A., 2006. The use of remote-sensing data for mass-balance studies at Myrdalsjokull ice cap, Iceland. J. Glaciol. 52 (179), 565–573.

König, M., Winther, J.-G., Knudsen, N.T., Guneriussen, T. (2000). Equilibrium- and firn-line detection with multi-polarization sar – first results. In The European Association of Remote Sensing Laboratories (EARSeL)-*Special Interest Groups (SIG) - Workshop Land Ice and Snow* (pp. 273–280). Dresden.

Kulkarni, A.V, Dhar, S., Rathore, B.P. et. Al., (2006). Recession of Samudra Tapu glacier, Chandra river basin, Himachal Pradesh. *J Indian Soc Remote Sens* 34(1):39–46. https://doi.org/10.1007/BF02990745.

Kumar, V., Venkataramana, G., & Høgda, K. a. (2011). Glacier surface velocity estimation using SAR interferometry technique applying ascending and descending passes in Himalayas. *International Journal of Applied Earth Observation and Geoinformation*, *13*(4), 545–551. http://doi.org/10.1016/j.jag.2011.02.004.

König, M., Winther, J., Isaksson, E., 2001. Measuring snow and glacier ice properties from satellite. Reviews of Geophysics 39 (1), 1–27.

Lee, E., Carrivick, J.L., Quincey, D.J., Cook, S.J., James, W.H., Brown, L.E., 2021. Accelerated mass loss of Himalayan glaciers since the Little Ice Age. Sci. Rep. 11 (1), 1–8.

Lee, J.-S., Pottier, E., 2009. Polarimetric Radar Imaging: From Basics to Applications. CRC Press Taylor and Francis Group, Boca Raton London New York.

Li, S., Benson, C., Gens, R., Lingle, C., 2008. Motion patterns of Nabesna Glacier (Alaska) revealed by interferometric SAR techniques. Remote Sens. Environ. 112 (9), 3628–3638. https://doi.org/10.1016/j.rse.2008.05.015.

López-Martínez, C., Pottier, E., 2021. Basic Principles of SAR Polarimetry. In: Hajnsek, I., Desnos, Y.L. (Eds.), Polarimetric Synthetic Aperture Radar. Remote Sensing and Digital Image Processing. 25. Springer, Cham. https://doi.org/10.1007/978-3-030-56504-6_1.

Luckman, A., Quincey, D., Bevan, S., 2007. The potential of satellite radar interferometry and feature tracking for monitoring flow rates of Himalayan glaciers. Remote Sens. Environ. 111, 172–181. https://doi.org/10.1016/j.rse.2007.05.019.

Mahagaonkar, A., Thakur, P.K., Chang, L., 2019. Assessment of Sentinel-1 Products for Revealing Glacier Surface Movement in Indian Himalayas Using Differential SAR Interferometry. *IGARSS 2019. IEEE Int. Geosci. Remote Sens. Sympos.,* Yokohama, Japan 2019, 2070–2073. https://doi.org/10.1109/IGARSS.2019.8898831.

Mandal, A., Ramanathan, A., Azam, M.F., Angchuk, T., Soheb, M., Kumar, N., Singh, V.B., 2020. Understanding the interrelationships among mass balance, meteorology, discharge and surface velocity on Chhota Shigri Glacier over 2002–2019 using in situ measurements. J. Glaciol. 66 (259), 727–741.

Mcnabb, R.W., Hock, R., Neel, S.O., Rasmussen, L.A., Ahn, Y., Braun, M., Truffer, M., 2012. Using surface velocities to calculate ice thickness and bed topography : a case study at Columbia Glacier, Alaska, USA. J. Glaciol. 58 (212), 1151–1164. https://doi.org/10.3189/2012JoG11J249.

Patel, L.K., Sharma, P., Singh, A.T., Pratap, B., Oulkar, S., Thamban, M., 2021. Spatial surface velocity pattern in the glaciers of Chandra Basin, Western Himalaya. *Geocarto Int.* 37 (18), 5327–5344. https://doi.org/10.1080/10106049.2021.1920627.

Paterson, W., 1994. Physics of Glaciers, 3rd ed. Oxford Elseveir Science Ltd, Chapter, p. 2.

Patrington, K.C., 1998. Discrimination of glacier facies using multi-temporal SAR data. J. Glaciol. 44 (146), 42–53.

Racoviteanu, A.E., Manley, W.F., Arnaud, Y., Williams, M.W., 2007. Evaluating digital elevation models for glaciologic applications: an example from Nevado Coropuna, Peruvian Andes. *Global Planet. Change* 59 (1–4), 110–125. https://doi.org/10.1016/j.gloplacha.2006.11.036.

Rau, F., Braun, M., Friedrich, M., et al., (2000) Radar glacier zones and their boundaries as indicators of glacier mass balance and climatic variability. *In: Proceedings of the EARSeL-LISSIG-workshop land ice and snow*, Dresden, Germany, 16–17 June 2000, 317–327.

Reigber, A., Scheiber, R., 2003. Airborne differential SAR interferometry : first results at L-Band. IEEE Trans. Geosci. Remote Sens. 41 (6), 1516–1520.

Rott, H., Matzler, C., 1987. Possibilities and limits of synthetic aperture radar for snow and glacier surveying. Ann. Glaciol. 9, 195–199.

Sahu, R., Gupta, R.D., 2019. Surface velocity dynamics of Samudra Tapu glacier, India from 2013 to 2017 using Landsat-8 data. ISPRS Ann. Photogramm., Remote Sens. Spatial Information Sci. 4, 75–81.

Sattar, A., Goswami, A., Kulkarni, A.V., Das, P., 2019. Glacier-surface velocity derived ice volume and retreat assessment in the Dhauliganga basin, central Himalaya–a remote sensing and modeling based approach. Front. Earth Sci. 7, 105.

Scherler, D., Leprince, S., Strecker, M., 2008. Glacier-surface velocities in alpine terrain from optical satellite imagery—accuracy improvement and quality assessment. Remote Sens. Environ. 112 (10), 3806–3819. https://doi.org/10.1016/j.rse.2008.05.018.

Shukla, A., Arora, M.K., Gupta, R.P., 2010. Synergistic approach for mapping debris-covered glaciers using optical–thermal remote sensing data with inputs from geomorphometric parameters. Remote Sens. Environ. 114 (7), 1378–1387. https://doi.org/10.1016/j.rse.2010.01.015.

Shuttle Radar Topography Mission. (2015). Retrieved from http://srtm.usgs.gov/.

Singh P, Singh VP (2001). *Snow and glacier hydrology.* Water science and technology, 37, Kluwer Academic Publishers, Dordrecht.

Singh, D.K., Thakur, P.K., Naithani, B.P., Dhote, P.R., 2021. Spatio-temporal analysis of glacier surface velocity in dhauliganga basin using geo-spatial techniques. Environ. Earth Sci. 80 (1), 1–16.

Singh, G., Yamaguchi, Y., Park, S.-E., 2011. Utilization of four-component scattering power decomposition method for glaciated terrain classification. Geocarto Int. 26 (5), 377–389. https://doi.org/10.1080/10106049.2011.584978.

Singh, G., Venkataraman, G., Yamaguchi, Y., Park, S.E., 2014. Capability assessment of fully polarimetric ALOS-PALSAR data for discriminating wet snow from other scattering types in mountainous regions. IEEE Trans. Geosci. Remote Sens. 52 (2), 1177–1196. https://doi.org/10.1109/TGRS.2013.2248369.

Small, D., Wemer, C., & Nuesch, D. (1993). Baseline modelling for ERS-1 SAR interferometry. *Geoscience and Remote Sensing Symposium, 1993.* IGARSS 93, 1203(1), 1204–1206.

Strozzi, T., Luckman, A., Murray, T., Wegmüller, U., Werner, C.L., 2002. Glacier motion estimation using SAR offset-tracking procedures. IEEE Trans. Geosci. Remote Sens. 40 (11), 2384–2391.

Thakur, P. K., Garg, V., Nikam, B. R., Singh, S., Jasmine, Chouksey, A., Dhote, P. R., Aggarwal, S. P., Chauhan, P., and Kumar, A. S. (2018). Snow Cover and Glacier Dynamics Study Using C-and L-Band SAR

Datasets in Parts of North West Himalaya. *Int. Arch. Photogramm. Remote Sens. Spatial Inf. Sci.,* XLII-5, 375-382, https://doi.org/10.5194/isprs-archives-XLII-5-375-2018.

Thakur, P.K., Swain, A.K., Dhote, P.R., Kumar, P., Kaushik, S., Gajbhiye, D., Mahagaonkar, A., Sharma, V., Dharwadkar, A., Aggarwal, S.P., Beg, J., Chauhan, P. and Kumar, A.S. (2021). Satellite and ground based estimates for ice surface velocities in the part of central Dronning Maud Land, East Antarctica: Implications for ice flux calculations. Polar Science, 30, p. 100737, 16 pages, https://doi.org/10.1016/j.polar.2021.100737.

Venkataraman, G., Singh, G., 2011. Radar application in Snow, Ice, and Glaciers Springer. Science. https://doi.org/10.1007/978-90-481-2642-2.

Wagnon, P., Linda, A., Arnaud, Y., Kumar, R., Sharma, P., Vincent, C., Chevallier, P., 2007. Four years of mass balance on Chhota Shigri Glacier, Himachal Pradesh, India, a new benchmark glacier in the western Himalaya. J. Glaciol. 53 (183), 603–611.

Winsvold, S.H., Kääb, A., Nuth, C., Andreassen, L.M., Van Pelt, W.J., Schellenberger, T., 2018. Using SAR satellite data time series for regional glacier mapping. The Cryosphere 12 (3), 867–890.

Yellala, A., Kumar, V., Høgda, K.A., 2019. Bara Shigri and Chhota Shigri glacier velocity estimation in western Himalaya using Sentinel-1 SAR data. Int. J. Remote Sens. 40 (15), 5861–5874.

Zhang, Y., Wang, Y., Chen, Y., Xu, Y., Zhang, G., Lin, Q., Luo, R., 2021. Projection of changes in flash flood occurrence under climate change at tourist attractions. J. Hydrol. 595 126039.

Zhou, Y., Hu, J., Li, Z., Li, J., Zhao, R., Ding, X., 2019. Quantifying glacier mass change and its contribution to lake growths in central Kunlun during 2000–2015 from multi-source remote sensing data. J. Hydrol. 570, 38–50.

Zongli, J., Shiyin, L., Sichun, L., Xin, W., 2012. Estimate Yengisogat Glacier Surface Flow Velocities Using ALOS PALSAR Data Feature-tracking, Karakoram, China. *Procedia Environ. Sci.* 12 (2006), 646–652. https://doi.org/10.1016/j.proenv.2012.01.330.